

H₂O and O₂ Absorption in the Coma of Comet 67P/Churyumov-Gerasimenko Measured by the Alice Far-Ultraviolet Spectrograph on *Rosetta*

Brian A. Keeney,¹★ S. Alan Stern,¹ Michael F. A’Hearn,² Jean-Loup Bertaux,³ Lori M. Feaga,² Paul D. Feldman,⁴ Richard A. Medina,¹ Joel Wm. Parker,¹ Jon P. Pineau,⁵ Rebecca Schindhelm,¹ Andrew J. Steffl,¹ M. Versteeg,⁶ and Harold A. Weaver⁷

¹Southwest Research Institute, Department of Space Studies, Suite 300, 1050 Walnut Street, Boulder, CO 80302, USA

²University of Maryland, Department of Astronomy, College Park, MD 20742, USA

³LATMOS, CNRS/UVSQ/IPSL, 11 Boulevard d’Alember, 78280 Guyancourt, France

⁴Johns Hopkins University, Department of Physics and Astronomy, 3400 N. Charles Street, Baltimore, MD 21218, USA

⁵Stellar Solutions, Inc., 250 Cambridge Ave., Suite 204, Palo Alto, CA 94306, USA

⁶Southwest Research Institute, 6220 Culebra Road, San Antonio, TX 78238, USA

⁷Johns Hopkins University Applied Physics Laboratory, 11100 Johns Hopkins Road, Laurel, MD 20723, USA

Accepted XXX. Received YYY; in original form ZZZ

ABSTRACT

We have detected H₂O and O₂ absorption against the far-UV continuum of stars located on lines of sight near the nucleus of Comet 67P/Churyumov-Gerasimenko using the Alice imaging spectrograph on *Rosetta*. These stellar appulses occurred at impact parameters of $\rho = 4\text{--}20$ km, and heliocentric distances ranging from $R_h = -1.8$ to 2.3 AU (negative values indicate pre-perihelion observations). The measured H₂O column densities agree well with nearly contemporaneous values measured by VIRTIS-H. The clear detection of O₂ independently confirms the initial detection by the ROSINA mass spectrometer; however, the relative abundance of O₂/H₂O derived from the stellar spectra (11%–68%, with a median value of 25%) is considerably larger than published values found by ROSINA. The cause of this difference is unclear, but potentially related to ROSINA measuring number density at the spacecraft position while Alice measures column density along a line of sight that passes near the nucleus.

Key words: comets: individual (67P) – ultraviolet: planetary systems

1 INTRODUCTION

One of the most significant results from the *Rosetta* mission to Comet 67P/Churyumov-Gerasimenko (67P/C-G) has been the persistent detection of O₂ in the coma (Bieler et al. 2015; Fougere et al. 2016) by the Double Focusing Mass Spectrometer (DFMS) of the Rosetta Orbiter Spectrometer for Ion and Neutral Analysis (ROSINA; Balsiger et al. 2007). The initial detection by Bieler et al. (2015) found that the relative number density of O₂ with respect to H₂O ranged from 1–10%, with a mean of $n_{\text{O}_2}/n_{\text{H}_2\text{O}} = 3.85 \pm 0.85\%$ for measurements taken between September 2014 and March 2015. Further modeling by Fougere et al. (2016) found that the relative production rate of O₂ with respect to H₂O is $\approx 1\text{--}2\%$

for measurements taken prior to February 2016. Both studies find that the number densities of O₂ and H₂O are highly correlated, with Pearson correlation coefficients > 0.8 .

Surprisingly, O₂ is the fourth most abundant species in the coma of 67P/C-G (behind H₂O, CO₂, and CO; Le Roy et al. 2015; Fougere et al. 2016), despite the fact that it had never been detected in a cometary coma before (Bieler et al. 2015). Subsequent reanalysis of mass spectrometer data from *Giotto*’s visit to Oort-Cloud Comet 1P/Halley has found that $n_{\text{O}_2}/n_{\text{H}_2\text{O}} = 3.7 \pm 1.7\%$ is consistent with the measurements (Rubin et al. 2015), suggesting that O₂ may be a common constituent of all comets, not just Jupiter Family Comets such as 67P/C-G. New theories are being developed to explain these O₂ detections, such as trapping O₂ in clathrates prior to agglomeration during comet formation (Mousis et al. 2016), astrochemical production of O₂ in dark

★ E-mail: bkeeney@gmail.com (BAK)

Table 1. Journal of Targeted Stellar Appulse Observations

Star	Sp. Type	Obs. Type	Date	UTC	Duration (min)	R_h (AU)	ϕ ($^\circ$)	θ ($^\circ$)	ρ (km)
HD 140008	B5 V	Appulse	2015 Dec 25	14:27:11	57	1.97	89.8	4.8-5.3	6.4-7.2
		Revisit 1	2016 Feb 29		37	2.47	92.9	88.3-88.9	
		Revisit 2	2016 Mar 12		39	2.56	91.9-92.0	87.0-88.0	
HD 144294	B2.5 V	Appulse	2015 Dec 25	15:37:11	111	1.97	89.8	9.9-10.8	13.3-14.6
		Revisit	2016 Mar 4		127	2.51	91.8	120.0-123.8	
HD 42933	B1/2 III	Appulse	2016 Jan 10	07:19:29	164	2.09	89.6	5.1-6.5	7.0-8.9
		Revisit 1	2016 Feb 29		51	2.47	92.9	171.1-171.8	
		Revisit 2	2016 Feb 29		77	2.48	92.6	172.9-173.8	
HD 89890	B5 II	Appulse	2016 Jan 18	13:28:59	169	2.16	60.4-60.5	12.1-12.9	17.1-18.2
		Revisit	2016 Mar 15		84	2.59	89.1	145.3-148.4	
HD 40111	B0/1 II/III	Appulse 1	2016 Jan 25	17:32:33	222	2.21	60.2-60.4	11.4-12.5	14.0-15.4
		Appulse 2	2016 Feb 9	19:38:27	170	2.33	64.9-65.6	8.8-9.8	7.8-8.6
		Revisit 1	2016 Feb 23		131	2.43	89.2-90.1	120.4-122.3	
		Revisit 2	2016 Feb 26		88	2.45	94.8	171.2-172.0	
HD 144206	B9 III	Appulse	2016 Feb 1	13:28:59	170	2.26	60.2-60.4	9.8-9.9	10.0-10.1
		Revisit	2016 Apr 1		62	2.71	112.1-112.9	177.8-178.7	

Notes. The phase angle is denoted by ϕ , and the off-nadir angle by θ . The last column lists the impact parameter, ρ .

clouds or forming protoplanetary disks (Taquet et al. 2016), and formation of O₂ during the evaporation of H₂O ice via dismutation of H₂O₂ (Dulieu, Minissale, & Bockelée-Morvan 2017).

In this Paper, we present H₂O and O₂ column densities measured along lines of sight to background stars projected near the nucleus of 67P/C-G by the Alice far-UV spectrograph (Stern et al. 2007). These stellar sight lines allow the coma of 67P/C-G to be studied in far-UV absorption, where column densities can be measured directly. Alice’s previous characterizations of the coma of 67P/C-G have primarily used emission lines from CO and atomic hydrogen, oxygen, carbon, and sulphur (e.g., Feldman et al. 2015, 2016). While the strengths of these emission lines can only be used to derive molecular column densities under specific assumptions (i.e., pure resonance fluorescence), the ratios of strong, commonly observed lines can be diagnostic of physical conditions in the coma. Feldman et al. (2016) inferred that O₂ was the primary driver of certain gaseous outbursts that exhibit a sudden increase in the O I λ 1356/ λ 1304 ratio in the sunward coma without any corresponding increase in dust production. Feldman et al. (2016) estimate that O₂/H₂O \geq 50% during these outbursts, substantially higher than the mean value of $3.85 \pm 0.85\%$ found by Bieler et al. (2015).

Several of *Rosetta*’s instruments are capable of measuring the abundance of H₂O (as well as CO and CO₂) in the coma of 67P/C-G. Most notably, ROSINA measures the number density of water, $n_{\text{H}_2\text{O}}$, at the spacecraft location using mass spectroscopy, while the Visible and Infrared Thermal Imaging Spectrometer (VIRTIS; Coradini et al. 2007) and the Microwave Instrument for the Rosetta Orbiter (MIRO; Gulbis et al. 2007) measure the column density of water, $N_{\text{H}_2\text{O}}$, along a specific line of sight using rotational and/or vibrational transitions. The UV-absorption spectra presented herein also allow Alice to directly measure $N_{\text{H}_2\text{O}}$, and facilitate comparisons with nearly contemporaneous measurements from ROSINA (Fougere et al. 2016) and VIRTIS-H (the high spectral resolution channel of VIRTIS; Bockelée-Morvan et al. 2016).

In contrast to the situation with H₂O, only Alice and ROSINA are capable of directly measuring O₂. This makes the observations reported herein an important and unique confirmation of the initial O₂ detections (Bieler et al. 2015). However, direct comparisons between ROSINA’s *in-situ* measurements and Alice’s measurements along specific lines of sight are not straightforward. The remainder of this Paper is organized as follows: the Alice spectrograph and stellar spectra are described in Section 2; H₂O and O₂ column densities are derived in Section 3; our values are compared with ROSINA and VIRTIS-H measurements in Section 4; and our conclusions are presented in Section 5.

2 STELLAR APPULSE OBSERVATIONS

Alice is a low-power, lightweight far-UV imaging spectrograph funded by NASA for inclusion on the ESA *Rosetta* orbiter (Stern et al. 2007). It covers the wavelength range 750-2050 Å with a spectral resolution of 8-12 Å, and has a slit that is 6° long, and narrower in the center (0°05 wide) than the edges (0°1 wide; Stern et al. 2007). Over the course of *Rosetta*’s orbital escort mission, Alice probed the sunward coma of 67P/C-G in absorption 30 times using UV-bright stars located along lines of sight near the nucleus as background sources. Here we report on the 29 observations (“appulses”) that were not occulted by the nucleus; we will report the details of our single stellar occultation separately (B. Keeney et al., in prep).

Quantifying the nature of the cometary coma required re-observing, or “revisiting”, these stars when they were far from the nucleus to characterize their intrinsic stellar spectra. This allowed us to isolate the coma absorption signature from the combined background effects of the stellar continuum and interstellar absorption. Further, there are two varieties of appulse observations, which we term “targeted” and “archival” appulses.

For the targeted appulses, we actively searched during operations planning for upcoming opportunities where a known bright star would be located within a few degrees

Table 2. Journal of Archival Stellar Appulse Observations

Star	Sp. Type	Obs. Type	Date	UTC	Duration (min)	R_h (AU)	ϕ (°)	θ (°)	ρ (km)
HD 26912	B3 IV	Appulse	2015 Apr 30	02:00:27	18	-1.75	72.5-72.6	1.7	4.5
		Revisit	2016 Mar 26		95	2.67	128.7-131.5	77.7-80.0	
HD 3901	B2 V	Appulse	2015 May 3	21:32:21	11	-1.72	60.3	1.7	4.0
		Revisit	2016 Aug 5		12	3.52	—	44.9	
HD 29589	B8 IV	Appulse	2015 May 27	03:19:43	46	-1.55	65.9	1.3	7.1
		Revisit	2016 Jul 22		24	3.44	88.8	99.0	
HD 174585	B3 IV	Appulse	2015 Jun 8	00:40:54	16	-1.48	87.4	1.5	5.4
		Revisit	2016 Aug 5		12	3.52	90.1	92.9	
HD 180554	B4 IV	Appulse	2015 Jun 28	00:16:04	4	-1.36	89.2	2.4	7.7
		Revisit	2016 Aug 5		12	3.52	92.6	96.9	
HD 191692	B9.5 III	Appulse	2015 Jul 12	22:59:29	14	-1.30	88.8	2.5	6.8
		Revisit	2016 Apr 19		17	2.84	86.4	35.2	
HD 195810	B6 III	Appulse	2015 Jul 25	08:56:47	11	-1.26	90.0	2.0	6.5
		Revisit	2016 Apr 19		17	2.84	86.5	41.1	
HD 192685	B3 V	Appulse	2015 Jul 26	08:54:44	11	-1.26	89.9	2.5	7.4
		Revisit	2016 Jun 27		17	3.29	93.8	99.9	
HD 68324	B2 V	Appulse	2015 Aug 9	19:39:33	20	-1.24	89.0	1.3	7.0
		Revisit	2016 Jun 6		30	3.15	67.9-68.2	88.2-88.4	
HD 66006	B2/3	Appulse	2015 Aug 10	04:28:49	21	-1.24	89.0	1.0	5.7
		Revisit	2016 Jun 6		31	3.15	69.1-69.5	86.6-87.0	
HD 64722	B2 IV	Appulse	2015 Aug 10	18:45:04	25	-1.24	89.2	2.5	14.2
		Revisit	2016 Jun 27		21	3.29	93.8	47.7-48.1	
HD 39844	B6 V	Appulse	2015 Aug 13	00:57:11	14	1.24	89.3	2.2	12.6
		Revisit	2016 Jun 27		17	3.29	93.8	35.4	
HD 207330	B3 III	Appulse	2015 Aug 27	03:18:10	12	1.26	79.7	1.5	10.4
		Revisit	2016 Apr 4		116	2.67	83.1-83.3	149.5-150.8	
HD 109387	B6 III	Appulse	2015 Sep 1	07:04:57	10	1.27	70.4	1.2	8.6
		Revisit	2016 Jun 5		22	3.15	85.3-85.6	135.2-135.7	
HD 124771	B3 V	Appulse	2015 Sep 10	04:52:33	12	1.29	119.9	3.6	20.1
		Revisit	2016 Jun 6		18	3.15	68.8	50.0	
HD 21428	B3 V	Appulse	2015 Nov 2	16:07:12	10	1.58	60.2	2.8	12.8
		Revisit	2016 Aug 5		12	3.52	94.9	28.2	
HD 32249	B3 IV	Appulse	2015 Nov 6	06:42:59	9	1.60	61.3	2.6	10.7
		Revisit	2016 Jul 22		9	3.44	88.9	77.1	
HD 33328	B2 IV	Appulse	2015 Nov 6	09:41:26	4	1.60	61.6	1.4	5.9
		Revisit	2016 Jul 22		9	3.44	88.7	81.6	
HD 106625	B8 III	Appulse	2015 Nov 13	08:16:25	6	1.65	61.1	1.6	4.7
		Revisit	2016 Jul 22		24	3.44	89.1	70.7	
HD 27376	B9 V	Appulse	2015 Nov 27	22:04:50	8	1.76	90.0	3.4	8.1
		Revisit	2016 Jul 22		14	3.44	88.9	48.7	
HD 23466	B3 V	Appulse	2015 Dec 16	22:38:45	7	1.90	89.8	2.9	5.2
		Revisit	2016 Aug 2		12	3.51	78.5	60.3	
HD 144217	B1 V	Appulse	2015 Dec 26	06:30:02	8	1.98	89.8	3.2	4.4
		Revisit	2016 Aug 5		12	3.52	91.5	130.4	

Notes. The phase angle is denoted by ϕ , and the off-nadir angle by θ . The last column lists the impact parameter, ρ .

of the nucleus. Inertial pointings were designed that facilitated long stares at these stars during the appulses, at the expense of a time-varying distance to the nucleus over the course of each observation. These targeted appulses were observed between 2015 Dec 25 and 2016 Feb 1 at heliocentric distances of $R_h = 1.97$ -2.26 AU, and are characterized by long exposure times (typically 12 Alice spectral images with exposure times of 10-20 minutes each were obtained per appulse), large off-nadir angles ($\theta \approx 5$ -10°), and large R_h compared to their archival counterparts.

To complement the targeted appulses, we also searched the extensive Alice archive (~ 40,000 exposures include the nucleus in the field-of-view) for instances where we serendipitously observed a UV-bright star near the nucleus as part

of normal operations. This search returned hundreds of candidates that were prioritized by the star's brightness and proximity to the nucleus, as well as the duration of the appulse and its proximity to the comet's perihelion passage on 2015 Aug 12, when coma activity was near its peak (Fougere et al. 2016). Since our typical pointing during normal operations was fixed with respect to the nucleus (i.e., not an inertial reference frame), we do not know the exact duration of the archival appulses because the star is moving with respect to the slit; however, we can estimate their durations with uncertainties of ~ 10% using NAIF/SPICE (Acton 1996). The archival appulses were observed between 2015 Apr 29 and 2015 Dec 26 at $R_h = 1.24$ -1.98 AU, and typically have shorter durations (10-20 min), smaller off-nadir angles ($\theta < 5^\circ$), and

smaller R_h than their targeted counterparts. However, the smaller off-nadir angles for the archival appulses are somewhat counteracted by the large spacecraft-comet distance, Δ , near perihelion, which led to similar impact parameters ($\rho = \Delta \sin \theta \approx 5\text{--}20$ km) for all appulses.

Table 1 and Table 2 list the properties of the 7 targeted and 22 archival appulses, respectively. The following information is listed by column: (1) the name of the star; (2) the stellar type and luminosity class as listed by SIMBAD (Wenger et al. 2000); (3) the observation type (either ‘‘appulse’’ or ‘‘revisit’’); (4) the date of observation; (5) the total exposure time, in minutes; (6) the heliocentric distance, R_h , in AU, where negative values indicate that the observation occurred prior to perihelion on 2015 Aug 12; (7) the phase angle, ϕ , in degrees; (8) the off-nadir angle, θ , in degrees; and (9) the impact parameter, ρ , in km. The impact parameter is only listed for appulse observations, not revisits, and the entries are ordered by appulse date.

Appulse observations have small off-nadir angles by construction ($\theta = 0^\circ$ implies we are looking straight at the nucleus), and revisits were constrained to have $\theta > 30^\circ$, although most were acquired when $\theta > 90^\circ$. Most of the appulses and revisits were observed at $\approx 90^\circ$ phase, with occasional deviations up to $\pm 30^\circ$ from this value. Note that one of the targeted stars, HD 40111, has two distinct appulses separated by ~ 2 weeks (see Table 1).

All exposures for a given appulse or revisit were flux-calibrated using spectrophotometric standard stars. Stellar spectra were then extracted from the spectral images and background subtracted. Spectra extracted from individual exposures were combined to improve the signal-to-noise ratio after first being normalized to have the same median flux from 1800–1900 Å. This range was chosen because both H₂O and O₂ have very small absorption cross sections in this region (Chung et al. 2001; Yoshino et al. 2005), but the stellar spectra still have sufficient signal-to-noise to allow a robust flux measurement (the effective area of Alice decreases rapidly for wavelengths > 1800 Å; Stern et al. 2007).

Next, the co-added revisit spectrum was scaled to have the same median flux from 1800–1900 Å as the co-added appulse spectrum. Finally, the appulse spectrum was divided by the scaled revisit (i.e., unocculted) spectrum to create a normalized spectrum in which the intrinsic stellar flux and interstellar absorption have been removed and only the differences in foreground coma absorption between the appulse and revisit spectra remain. By normalizing the spectra in this manner we also make ourselves insensitive to the uncertainty in the amount of time the star was in the slit.

Figure 1

displays co-added revisit spectra for three main sequence stars that span the range of stellar types observed. All three stars have sufficient flux at $\lambda > 1400$ Å to create normalized spectra with reasonable signal-to-noise, but the early- and mid-type *B* stars have considerably more flux at shorter wavelengths than the late-type *B* star does. Thus, normalized spectra for late-type appulse stars are inherently noisier at bluer wavelengths than normalized spectra for earlier-type stars.

We note that in a few cases we normalized the spectra from 1400–1450 Å when normalization from 1800–1900 Å was problematic. While 1400–1450 Å has small H₂O absorption cross sections (Chung et al. 2001), it is the region where O₂

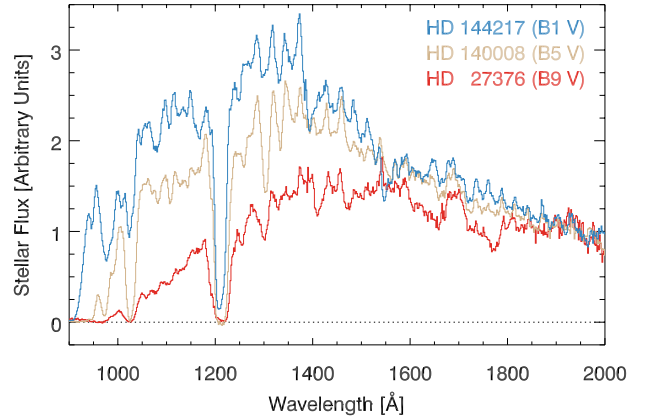


Figure 1. Revisit spectra for three main sequence stars. The spectra are normalized to have the same flux from 1800–1900 Å to emphasize the differences between early- and late-type *B* stars at far-UV wavelengths.

absorption cross sections are largest (Yoshino et al. 2005). The 1400–1450 Å region is therefore not ideal for spectral normalization, since using it reduces our sensitivity for O₂ absorption. Fits to spectra where we had to use this normalization region are not used for detailed analyses (see Section 3 for details).

3 ANALYSIS OF H₂O AND O₂ ABSORPTION

We have searched for optically-thin absorption from H₂O and O₂ in the normalized stellar spectra as described above. For a given molecule, i , we model the optical depth, τ_i , as a function of wavelength, λ , as:

$$\tau_i(\lambda) = N_i \sigma_i(\lambda), \quad (1)$$

where N_i is the column density of species i and $\sigma_i(\lambda)$ is the absorption cross section of species i as a function of wavelength. Combining absorption from several different species yields an expected (normalized) model flux of

$$F(\lambda) = e^{-\sum \tau_i(\lambda)}. \quad (2)$$

This model spectrum can then be compared to the normalized stellar spectrum to constrain the column densities of interest.

Table 3 lists the ten species that we model in our analysis. While we are primarily interested in H₂O and O₂, other abundant species must be included to robustly constrain the range of permissible H₂O and O₂ column densities. All species with $> 0.5\%$ abundance relative to H₂O in the coma of 67P/C-G in Le Roy et al. (2015) with available far-UV absorption cross sections are tabulated. Table 3 lists the following information by column: (1) species; (2) wavelength range; (3) measurement temperature; and (4) measurement reference. The adopted cross sections were downloaded from the PHoto Ionization/Dissociation RATES website¹ (Huebner & Mukherjee 2015); for most species, they are composites of several different measurements covering the wavelength range 900–2000 Å. The molecular cross sections in Table 3 are displayed in Figure 2.

¹ <http://phidrates.space.swri.edu>

Table 3. Molecular Cross Sections

Species	λ (Å)	T (K)	Reference
H_2O	1400-1898	250	Chung et al. (2001)
	1148-1939	298	Mota et al. (2005)
	850-1110	298	Watanabe & Jursa (1964)
O_2	1060-1860	298	Watanabe & Zelikoff (1953)
	1300-1752	295	Yoshino et al. (2005)
	41-1771	298	Brion & Tan (1979)
CO	1163-2000	298	Ackerman et al. (1970)
	584-1038	298	Cairns & Samson (1965)
CO ₂	1061-1187	295	Stark et al. (2007)
	1187-1755	295	Yoshino et al. (1996)
CH ₄	61-1450	298	Chan et al. (1993)
	155-1550	298	Hitchcock et al. (1980)
	1380-1600	295	Mount & Moos (1978)
C ₂ H ₂	952-1306	295	Sun & Weissler (1955)
	773-1370	298	Ditchburn (1955)
C ₂ H ₆	1050-2011	298	Nakayama & Watanabe (1964)
	600-1000	298	Metzger & Cook (1964)
C ₂ H ₄	1380-1600	295	Mount & Moos (1978)
	1200-1380	298	Okabe & Becker (1963)
	1160-1200	298	Lombos et al. (1967)
C ₄ H ₂	354-1127	—	Koch & Skibowski (1971)
	500-1200	—	Schoen (1962)
H ₂ CO	1065-1960	—	Zelikoff & Watanabe (1953)
	1210-1730	296	Okabe (1981)
H ₂ CO	1600-2600	295	Fahr & Nayak (1994)
	600-1760	—	Mentall et al. (1971)
H ₂ CO	1760-1850	—	Gentieu & Mentall (1970)

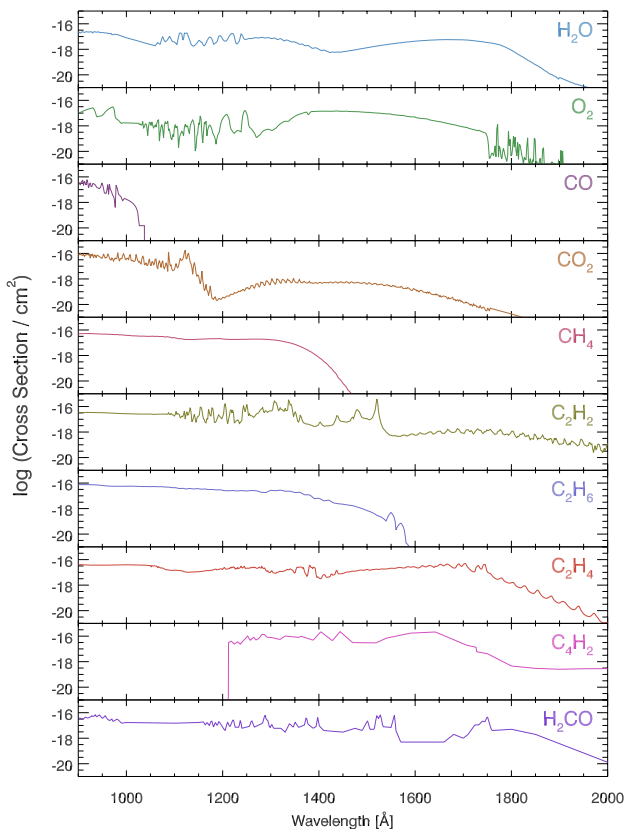


Figure 2. Molecular absorption cross sections used in this work.

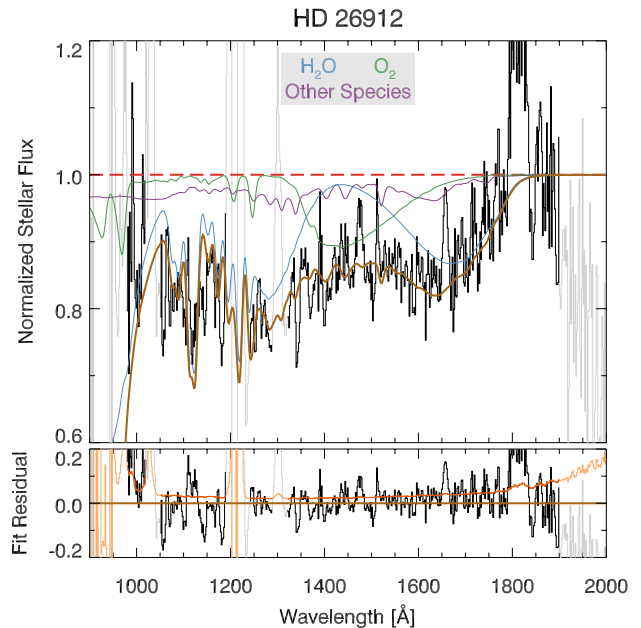


Figure 3. Fits to the appulse absorption of HD 26912 (FQ = 2). *Top:* The normalized stellar flux (black) with best-fit ensemble absorption (brown) overlaid. Individual absorption from H_2O (blue), O_2 (green), and other species (purple; ensemble sum of CO, CO₂, CH₄, etc. from Table 3) are also shown. *Bottom:* The residual of the ensemble fit, with 1σ flux uncertainty (orange) overlaid. Masked regions are shown in lighter hues in both panels; these regions are not used to constrain the fits. Absorption fits for all targeted and archival stellar appulses are shown in Appendix A.

All of the cross section measurements were performed near room temperature and laboratory measurements are not consistently available for all species in Table 3 at any other temperature; however, the gas kinetic temperature in the coma of 67P/C-G varies considerably. Barucci et al. (2016) found that exposed water ice on the nucleus has $T \approx 160$ -220 K, while Lee et al. (2015) found that the temperature of the coma decreases as $T \propto \rho^{-1}$ until it reaches a terminal temperature of $T \approx 50$ -75 K. The discrepancy between the temperature of the gas whose cross section was measured and the temperature of the absorbing coma gas introduces a systematic uncertainty in our modeling procedure. The peak O_2 cross section decreases by ~ 0.1 dex as the temperature decreases from 295 to 78 K (Yoshino et al. 2005); thus, by assuming room-temperature cross sections we are systematically under-estimating the O_2 column density required to match the observed absorption. Unfortunately, no H_2O cross sections are available at $T < 250$ K, so we are unable to estimate the magnitude of the systematic variation in O_2/H_2O .

We estimate the molecular column densities using non-linear least-squares regression of Equation 2 with MPFIT² (Markwardt 2009). The free parameters of the fit are the logarithm of the H_2O column density, in units of cm^{-2} , and the relative column densities of O_2 , CO, CO₂, etc. with re-

² <http://purl.com/net/mpfit>

Table 4. Stellar Appulse Column Densities

Star	S/N	FQ	<i>Best-Fit Values</i>		<i>Adopted Values</i>	
			$\log N_{\text{H}_2\text{O}}$	$\text{O}_2/\text{H}_2\text{O}$	$\log N_{\text{H}_2\text{O}}$	$\text{O}_2/\text{H}_2\text{O}$
HD 26912	33	2	16.40 ± 0.01	0.327 ± 0.024	16.40 ± 0.04	0.315 ± 0.056
HD 3901	19	4	16.16 ± 0.02	0.000	16.14 ± 0.09	< 0.179
HD 29589	48	2	17.03 ± 0.01	0.442 ± 0.015	17.03 ± 0.03	0.435 ± 0.046
HD 174585	17	3	16.49 ± 0.02	0.038 ± 0.021	16.49 ± 0.06	< 0.155
HD 180554	13	4	16.37 ± 0.03	0.000	16.36 ± 0.09	< 0.164
HD 191692	28	2	16.76 ± 0.01	0.123 ± 0.009	16.76 ± 0.04	0.123 ± 0.035
HD 195810	27	2	16.80 ± 0.01	0.223 ± 0.013	16.80 ± 0.04	0.219 ± 0.040
HD 192685	30	1	16.75 ± 0.01	0.087 ± 0.014	16.75 ± 0.04	< 0.123
HD 68324	45	2	16.85 ± 0.01	0.161 ± 0.016	16.85 ± 0.03	0.155 ± 0.042
HD 66006	39	1	17.08 ± 0.01	0.111 ± 0.009	17.08 ± 0.03	0.109 ± 0.030
HD 64722	37	2	16.76 ± 0.01	0.324 ± 0.015	16.76 ± 0.03	0.321 ± 0.044
HD 39844	14	2	16.73 ± 0.01	0.188 ± 0.013	16.72 ± 0.05	0.190 ± 0.048
HD 207330	39	2	16.80 ± 0.01	0.150 ± 0.010	16.80 ± 0.04	0.149 ± 0.033
HD 109387	27	1	16.78 ± 0.01	0.154 ± 0.013	16.78 ± 0.04	0.151 ± 0.041
HD 124771	24	1	16.56 ± 0.01	0.288 ± 0.017	16.55 ± 0.04	0.285 ± 0.049
HD 21428	20	4	15.81 ± 0.03	0.000	15.82 ± 0.12	< 0.272
HD 32249	28	2	16.50 ± 0.01	0.569 ± 0.025	16.50 ± 0.04	0.560 ± 0.066
HD 33328	25	2	16.47 ± 0.01	0.128 ± 0.023	16.46 ± 0.04	< 0.167
HD 106625	49	1	16.72 ± 0.01	0.309 ± 0.009	16.72 ± 0.04	0.308 ± 0.031
HD 27376	23	3	16.18 ± 0.03	0.000	16.16 ± 0.09	< 0.145
HD 23466	15	4	16.07 ± 0.04	0.000	16.06 ± 0.11	< 0.224
HD 140008	49	2	15.95 ± 0.03	0.355 ± 0.048	15.94 ± 0.06	0.334 ± 0.072
HD 144294	102	3	15.63 ± 0.02	0.590 ± 0.069	15.61 ± 0.05	0.563 ± 0.089
HD 144217	53	3	16.00 ± 0.03	0.000	15.98 ± 0.08	< 0.116
HD 42933	119	3	15.60 ± 0.02	0.441 ± 0.050	15.58 ± 0.05	0.412 ± 0.081
HD 89890	62	4	15.33 ± 0.04	1.000	15.30 ± 0.11	> 0.733
HD 40111 (A)	86	3	15.59 ± 0.02	0.702 ± 0.053	15.57 ± 0.06	0.678 ± 0.089
HD 144206	35	2	15.80 ± 0.03	0.521 ± 0.056	15.78 ± 0.08	0.495 ± 0.092
HD 40111 (B)	76	3	15.27 ± 0.04	0.297 ± 0.060	15.18 ± 0.12	< 0.338

Notes. Entries are ordered chronologically, and all column densities have units of cm^{-2} . Uncertainties are quoted at the 1σ level, and limits are quoted at the 3σ level.

spect to water (e.g., $\text{O}_2/\text{H}_2\text{O} \equiv N_{\text{O}_2}/N_{\text{H}_2\text{O}}$). The O_2 , CO , and CO_2 columns are constrained to lie in the range 0-100% relative to H_2O , and all other species are constrained to the range 0-1%. We model the wavelength range 950-1900 Å, with regions near strong coma emission lines (e.g., H I Ly α , H I Ly β , and the O I 1304 Å multiplet, where residuals from background subtraction are often present) and regions with very low S/N masked out. The fit to the appulse of HD 26912 is presented in Figure 3, which shows the normalized stellar spectrum compared to ensemble and individual-species absorption in the top panel, and the ensemble fit residual in the bottom panel. Fits to all targeted and archival appulses are presented in Appendix A.

The best-fit values of $\log N_{\text{H}_2\text{O}}$ and $\text{O}_2/\text{H}_2\text{O}$ for all of the stellar appulses are shown in Table 4, which lists the following information by column: (1) star name; (2) median S/N in the wavelength range 1250-2000 Å; (3) Fit Quality (FQ) flag; (4) logarithm of the best-fit H_2O column density, in cm^{-2} ; (5) best-fit value of the relative column density of O_2 relative to H_2O ; (6) logarithm of the adopted H_2O column density, in cm^{-2} ; and (7) adopted value of the relative column density of O_2 relative to H_2O . The “adopted” values in Columns 6 and 7 are described in more detail in Section 3.1. All quantities in Columns 4-7 are listed with 1σ uncertainties.

The FQ flag in Column 3 is a subjective measure of the quality of the absorption line fit for a given star, with

lower values indicating higher quality. Stars with FQ = 1 are reasonably fit over the full wavelength range 900-2000 Å (see Figure A8). Stars with FQ = 2 have some regions of very low S/N (see Figure A6), or mild discrepancies between the observed and model fluxes (see Figure A3). Stars with FQ = 3 have large regions with systematic discrepancies between the observed and model fluxes. All stars that were normalized from 1400-1450 Å instead of the default 1800-1900 Å region (see Section 2) were assigned FQ = 4. We also assigned FQ = 4 to the appulse of HD 89890, whose fit preferred $N_{\text{O}_2} > N_{\text{H}_2\text{O}}$ and had systematic discrepancies throughout the fitting range. Only stars with FQ ≤ 3 are used in subsequent analyses.

There are two notable features of the best-fit column densities in Table 4. The first is that the formal fitting uncertainties are very small. The second is that the $\text{O}_2/\text{H}_2\text{O}$ values are considerably higher than those in Bieler et al. (2015), who found a mean value of $3.85 \pm 0.85\%$ over an approximately 7 month period when $R_h = -3.4$ to -2 AU. It is possible that seasonal variations can account for some of this difference since the dates of our appulses do not overlap with the dates of the Bieler et al. (2015) measurements. However, Bieler et al. (2015) find no evidence of systematically increasing $\text{O}_2/\text{H}_2\text{O}$ in their measurements, almost all of which have $\text{O}_2/\text{H}_2\text{O} < 0.1$, and several of the best-fit values in Table 4 have $\text{O}_2/\text{H}_2\text{O} > 0.5$.

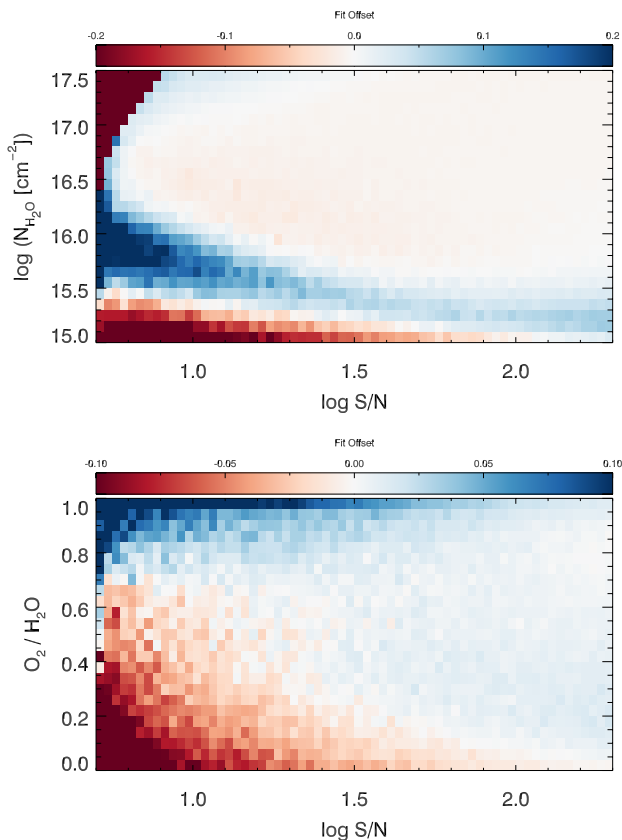


Figure 4. Average offsets between the true and best-fit values of $\log N_{\text{H}_2\text{O}}$ (*top*) and $\text{O}_2/\text{H}_2\text{O}$ (*bottom*) as a function of $\log \text{S/N}$. When $\text{S/N} > 10$, the magnitude of the $\log N_{\text{H}_2\text{O}}$ offset is typically $\lesssim 0.05$ dex, and the magnitude of the $\text{O}_2/\text{H}_2\text{O}$ offset is $\lesssim 0.02$.

3.1 Adopted Values of $N_{\text{H}_2\text{O}}$ and $\text{O}_2/\text{H}_2\text{O}$

We tested our fitting procedure by forward modeling simulated data with pre-defined, “true”, values of S/N , $N_{\text{H}_2\text{O}}$, and $\text{O}_2/\text{H}_2\text{O}$. We began with a flat-spectrum source ($F(\lambda) = 1$ at all wavelengths) upon which we superimposed H_2O absorption with a column density uniformly drawn from the range $15 < \log N_{\text{H}_2\text{O}} < 17.5$, O_2 , CO , and CO_2 absorption with a column density relative to water uniformly drawn from the range 0-100%, and CH_4 , C_2H_2 , C_2H_6 , C_2H_4 , C_4H_2 , and H_2CO absorption with a column density relative to H_2O uniformly drawn from the range 0-1%. These are the same ranges that were used in the fits to the appulse observations.

Next, we added to the spectrum Poisson noise that had a median S/N in the 1250-2000 Å range chosen uniformly from $0.7 < \log \text{S/N} < 2.3$, bracketing the observed values. A template for the S/N as a function of wavelength was derived from the revisit (i.e., unocculted) spectra of our appulse targets by normalizing each spectrum to have the same median S/N from 1250-2000 Å. Then at each wavelength we chose the median “normalized S/N ” value from all of the spectra to form the S/N profile of a “typical” appulse star. This template achieves peak S/N at ~ 1350 Å and varies by a factor of ~ 10 over the wavelength range 950-2000 Å.

This noisy, simulated spectrum was then treated just like the stellar appulse observations; i.e., it was normalized to have $\langle F(\lambda) \rangle = 1$ from 1800-1900 Å and then fit with the

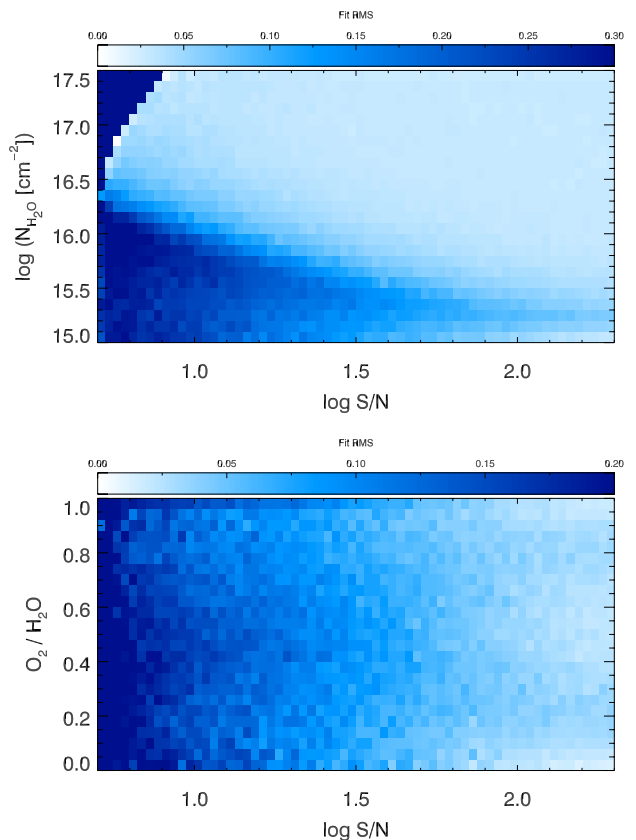


Figure 5. RMS deviations between the true and best-fit values of $\log N_{\text{H}_2\text{O}}$ (*top*) and $\text{O}_2/\text{H}_2\text{O}$ (*bottom*) as a function of $\log \text{S/N}$, after correcting for the systematic offsets in [Figure 4](#). When $\text{S/N} > 10$, the RMS of $\log N_{\text{H}_2\text{O}}$ is typically 0.05-0.10 dex, and the RMS of $\text{O}_2/\text{H}_2\text{O}$ is ~ 0.05 .

same procedure described above. The best-fit column densities and uncertainties were then saved along with the true values used to generate the simulated spectrum, and the process was repeated 500,000 times to thoroughly sample the full range of parameter space.

The best-fit and true values of $N_{\text{H}_2\text{O}}$ and $\text{O}_2/\text{H}_2\text{O}$ are compared as a function of S/N in [Figure 4](#). These images are two-dimensional histograms, where the color bars display the mean offset between the best-fit and true values in a given bin. Systematic offsets are present in both $N_{\text{H}_2\text{O}}$ and $\text{O}_2/\text{H}_2\text{O}$ when $\text{S/N} < 10$, but are quite modest at the higher S/N values typical of our appulse observations (see [Table 4](#)). [Figure 5](#) is similar to [Figure 4](#), except its color bars display the RMS deviations between the best-fit and true values in a given bin after correcting for the systematic offsets in [Figure 4](#). These deviations quantify the spread in true values that are associated with a particular best-fit value.

The “adopted” values of $N_{\text{H}_2\text{O}}$ and $\text{O}_2/\text{H}_2\text{O}$ are derived from our Monte Carlo simulations by identifying the 1,000 simulated spectra with S/N and best-fit values closest to those measured for a given observation, and fitting a Gaussian to the distribution of true values. We treat the mean of this Gaussian as the adopted value, and its standard deviation as the 1σ uncertainty. Since our fits constrain the allowable range of $\text{O}_2/\text{H}_2\text{O}$, we quote limits whenever the adopted value is $< 3\sigma$ from these boundaries.

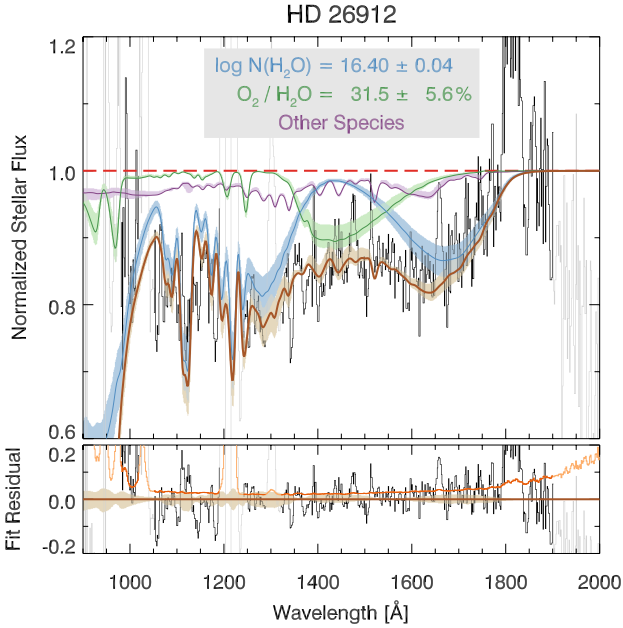


Figure 6. Adopted column densities for the appulse of HD 26912 (FQ = 2), with 95% (2σ) confidence bands. *Top*: The normalized stellar flux, with ensemble fit (brown) and individual-species absorption overlaid using the adopted column densities of H_2O and O_2 from Table 4. *Bottom*: The residual of the ensemble fit, with 1σ flux uncertainty (orange) overlaid. Masked regions are shown in lighter hues in both panels; these regions are not used to constrain the fits. Adopted column densities for all targeted and archival stellar appulses are shown in Appendix B.

The last two columns of Table 4 list the adopted values of $\log N_{\text{H}_2\text{O}}$ and $\text{O}_2/\text{H}_2\text{O}$, respectively, for our stellar appulse observations. Figure 6 shows absorption profiles of H_2O and O_2 and their associated 95% (2σ) confidence bands using the adopted values for the appulse of HD 26912. These profiles are overlaid on the normalized stellar spectrum as in Figure 3, along with confidence bands for the sum of all other modeled species and the total absorption from all species. These profiles clearly show that the adopted values of $\log N_{\text{H}_2\text{O}}$ and $\text{O}_2/\text{H}_2\text{O}$ are consistent with the data. Absorption profiles derived from the adopted values for all targeted and serendipitous appulses are presented in Appendix B.

4 DISCUSSION

4.1 H_2O Column Densities

The Monte Carlo simulations presented in Section 3.1 are one way to gain confidence in the validity of our absorption fits. Another is to compare our H_2O column densities with values measured by other instruments on *Rosetta* at similar times. Figure 7 shows the adopted values of $\log N_{\text{H}_2\text{O}}$ for our stellar appulse observations as a function of R_h , compared to the VIRTIS-H measurements of Bockelée-Morvan et al. (2016). Despite the large scatter in the column densities for a given value of R_h , the adopted values for our appulse observations are reassuringly similar to the measured values from VIRTIS. One reason for the differences that do exist is the fact that the VIRTIS measurements were taken at sys-

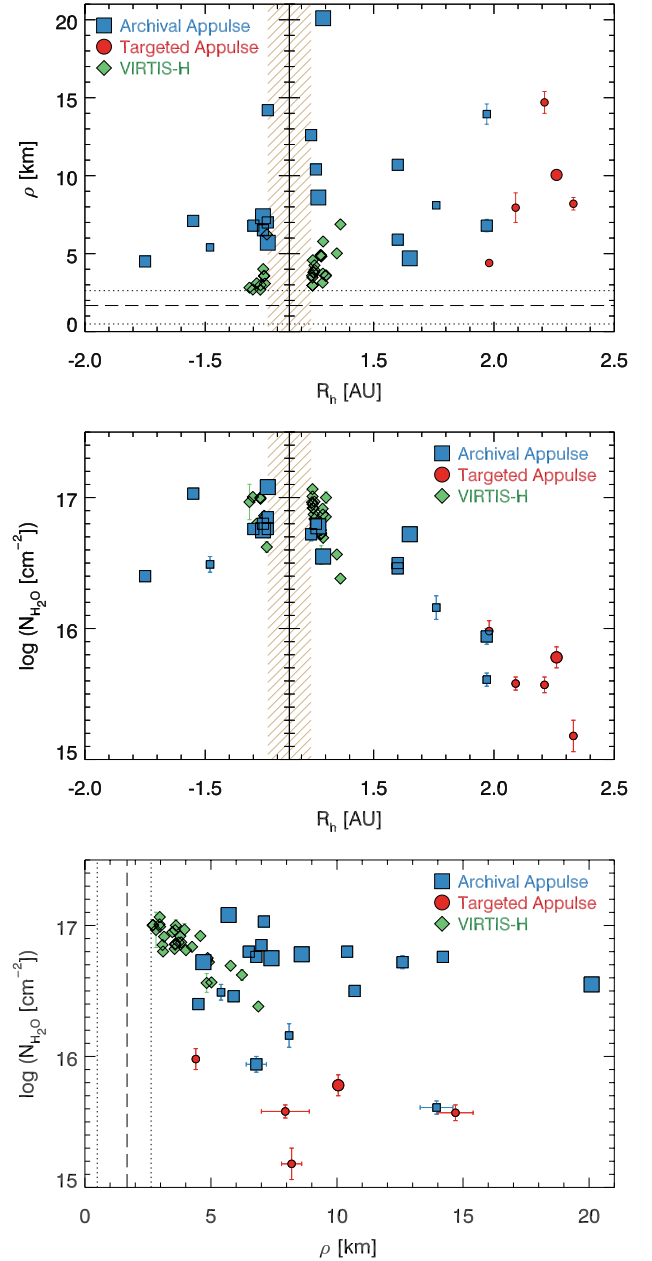


Figure 7. *Top*: Distribution of the stellar appulse observations with heliocentric radius (R_h) and impact parameter (ρ). *Middle*: Distribution of the adopted values of $N_{\text{H}_2\text{O}}$ with R_h . *Bottom*: Distribution of the adopted values of $N_{\text{H}_2\text{O}}$ with ρ . The VIRTIS-H measurements of Bockelée-Morvan et al. (2016) are also plotted in all three panels. Heliocentric distances in the beige hatched region are smaller than the perihelion distance of 1.24 AU. The dashed line in the top and bottom panels is the effective radius of the nucleus, and the dotted lines indicate its minimum and maximum radii. Symbol size encodes fit quality in all panels, with higher quality fits (lower FQ values) having larger symbols; points with no error bars have uncertainties smaller than the symbol size.

tematically lower impact parameters than the appulses, as shown in the top panel of Figure 7.

While the $N_{\text{H}_2\text{O}}$ values from Alice and VIRTIS are in good agreement, there may be discrepancies with the ROSINA measurements. Fougere et al. (2016) present a sophisticated Direct Simulation Monte Carlo (DSMC) model

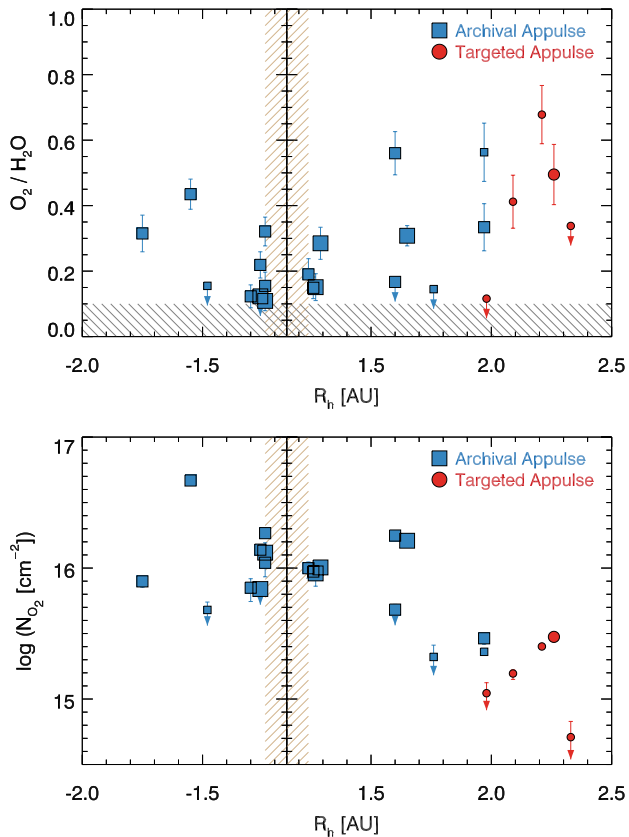


Figure 8. O_2/H_2O (top) and N_{O_2} (bottom) as a function of R_h . Symbol sizes are the same as in Figure 7. Heliocentric distances in the beige hatched region are smaller than the perihelion distance of 1.24 AU. The gray hatched region in the top panel indicates typical values of O_2/H_2O measured by ROSINA (Bieler et al. 2015; Fougere et al. 2016).

of the major species (H_2O , CO_2 , CO , and O_2) in the coma of 67P/C-G, which derives molecular production rates from a non-uniform surface activity distribution. The DSMC model does a remarkable job of reproducing the *in-situ* ROSINA measurements of the number density of these species for all data taken before March 2016 (Fougere et al. 2016). However, when the model production rates are used to predict the N_{H_2O} values along the lines of sight probed by Bockelée-Morvan et al. (2016), it finds model column densities that are four times higher than those measured by VIRTIS (Fougere et al. 2016). The cause of this discrepancy is unclear, which illustrates the difficulty of directly comparing measurements from *in-situ* instruments such as ROSINA to those from remote-sensing instruments such as VIRTIS and Alice.

4.2 O_2/H_2O

Figure 8 shows the relative abundance of O_2 with respect to H_2O (top panel) and the column density of O_2 (bottom panel) as a function of R_h . Figure 9 shows the same quantities as a function of impact parameter. The relative O_2/H_2O abundance tends to increase with increasing heliocentric distance and increasing impact parameter. These correlations (3.9σ and 2.5σ significance, respectively, according to Kendall’s tau test) cause the distributions of N_{O_2} as a

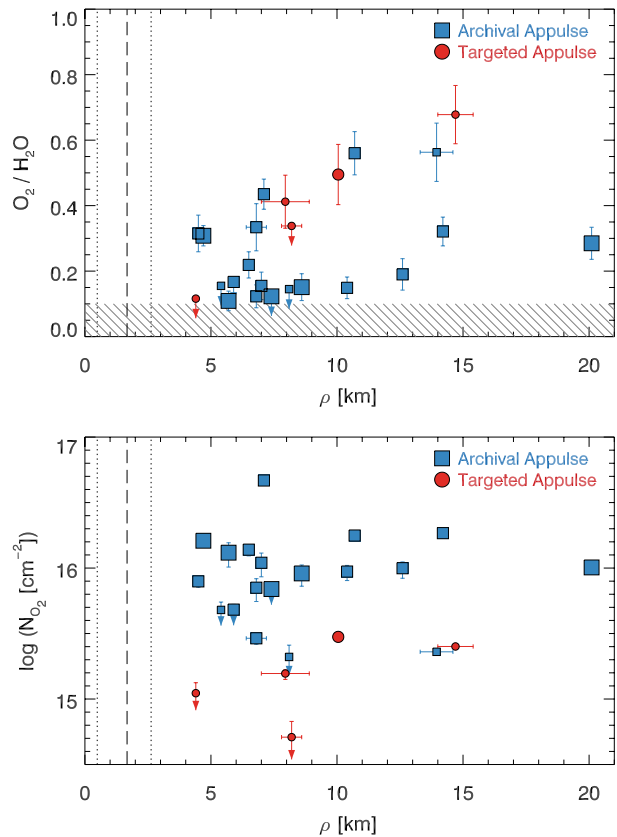


Figure 9. O_2/H_2O (top) and N_{O_2} (bottom) as a function of impact parameter. Symbol sizes are the same as in Figure 7. The dashed vertical line is the effective radius of the nucleus, and the dotted vertical lines indicate its minimum and maximum radii.

function of R_h and ρ to be flatter than the corresponding distributions of N_{H_2O} shown in Figure 7.

The relatively flat distribution of N_{O_2} as a function of ρ is particularly interesting, as it suggests a distributed source of O_2 . This would seem to argue against the variety of mechanisms that Mousis et al. (2016) suggest for trapping O_2 in the icy H_2O matrix of 67P/C-G. Formation of O_2 through the dismutation of H_2O_2 during the evaporation of H_2O ice, as suggested by Dulieu et al. (2017), might be able to explain the shape of the O_2/H_2O distribution as a function of ρ . Interestingly, ROSINA detects H_2O_2 in the coma of 67P/C-G (see Figure 4 of Le Roy et al. 2015, and Figure 4 of Bieler et al. 2015), but with a relative abundance of $H_2O_2/O_2 < 0.1\%$ (Bieler et al. 2015), far less than the ratio of $H_2O_2/O_2 = 2$ predicted by the dismutation reaction (Dulieu et al. 2017).

Feldman et al. (2016) used Alice to study gaseous outbursts in the coma of 67P/C-G. These outbursts exhibit no increase in long-wavelength solar reflected light that would indicate an increase in dust production, and are characterized by a sudden increase in the brightness ratio of $O\ I\ \lambda 1356/\lambda 1304$ in the sunward coma. Feldman et al. (2016) infer that these outbursts are driven by O_2 release, and estimate that $O_2/H_2O \geq 50\%$ during the outbursts.

Coincidentally, our earliest archival appulse (HD 26912; see Figure 3 and Figure 6) occurred during the onset of one of the Feldman et al. (2016) outbursts (see their Section 2.5).

We adopt $O_2/H_2O = 31.5 \pm 5.6\%$ for this appulse (see Table 4), which is somewhat lower than the Feldman et al. (2016) estimate. This apparent discrepancy is likely a result of timing differences; i.e., the adopted value from the appulse measures the ambient O_2/H_2O in the coma just prior to outburst, whereas the Feldman et al. (2016) value measures the peak O_2/H_2O over the ~ 30 -minute duration of the outburst.

As mentioned in Section 3, the O_2/H_2O values in Table 4 are generally higher, and have considerably larger scatter, than the values found by ROSINA-DFMS. Bieler et al. (2015) found $n_{O_2}/n_{H_2O} = 3.85 \pm 0.85\%$ in data taken between August 2014 and March 2015, and Fougere et al. (2016) found $Q_{O_2}/Q_{H_2O} \approx 2\%$ throughout the time frame of our appulse observations. Notably, neither Bieler et al. (2015) nor Fougere et al. (2016) list a single observation where $O_2/H_2O > 15\%$, but we find a median value of 25%.

As discussed in Section 4.1, comparisons between the *in-situ* measurements of ROSINA and the line-of-sight measurements of Alice and VIRTIS are not straightforward, even with a sophisticated coma model (Fougere et al. 2016). Nonetheless, the large values of O_2/H_2O derived from the Alice data are surprising. While we have included several minor species in our absorption fits (see Section 3), there are many species detected in the coma of 67P/C-G by ROSINA for which we were unable to find absorption cross sections (e.g., HS, S₂, CH₄O; Le Roy et al. 2015). Some of these “missing” species could have cross sections large enough to cause measurable far-UV absorption, even for very small column densities, causing the current O_2/H_2O values to be over-estimated. Quantifying the magnitude of these systematic uncertainties is exceedingly difficult without additional laboratory data for far-UV molecular absorption cross sections.

Further, even if our fits currently include all of the relevant species, the absorption cross sections we use were all measured at $T \approx 300$ K (see Table 3). Since the absorbing coma gas is expected to be at lower temperature, variations in the absorption cross sections with temperature could lead us to infer incorrect values of the column density with our current procedure. However, the scant existing data suggest that our procedure under-estimates the amount of low-temperature O_2 present by assuming room-temperature cross sections (see discussion in Section 3; Yoshino et al. 2005), which would serve to increase the discrepancy between our results and those of ROSINA.

5 CONCLUSIONS

Using the Alice far-UV imaging spectrograph aboard *Rosetta*, we have independently verified the presence of O_2 in the coma of Comet 67P/C-G. O_2 was detected for the first time in the coma of a comet by *Rosetta*’s ROSINA mass spectrometer (Bieler et al. 2015; Fougere et al. 2016). In the present study, both O_2 and H_2O were detected in far-UV absorption against the continuum of stars located near the nucleus of 67P/C-G, at impact parameters of 4-20 km. These stellar appulses occurred at heliocentric distances of -1.8 to 2.3 AU, where negative distances indicate pre-perihelion observations. The main results of our analysis are as follows:

(i) The H_2O column densities derived from the stellar

spectra are in good agreement with VIRTIS-H measurements from the same time period taken at similar impact parameters (Bockelée-Morvan et al. 2016).

(ii) The median value for the relative abundance of O_2 with respect to H_2O derived from the stellar spectra is $O_2/H_2O = 25\%$. This value is considerably higher than those reported by ROSINA; Bieler et al. (2015) and Fougere et al. (2016) found mean values of $O_2/H_2O < 5\%$.

We see no simple explanation for the difference in O_2/H_2O measured by Alice and ROSINA, unless it is related to the unmodeled species and $T = 300$ K cross sections discussed at the end of Section 4.2. The Alice H_2O measurements are consistent with values published by other remote-sensing instruments on *Rosetta*; and while this does not guarantee that our O_2 values are correct it does suggest that our measurements are reasonably robust. The ROSINA measurements, on the other hand, are performed *in situ* at the spacecraft location, and the sophisticated coma model of Fougere et al. (2016) is designed to reproduce these measurements. This same model has difficulty reproducing the H_2O column densities of Bockelée-Morvan et al. (2016), which were measured very close to perihelion (Fougere et al. 2016). There is clearly much future work to be done to reconcile these differences.

ACKNOWLEDGEMENTS

Rosetta is an ESA mission with contributions from its member states and NASA. We thank the members of the *Rosetta* Science Ground System and Mission Operations Center teams, in particular Richard Moissl and Michael Küppers, for their expert and dedicated help in planning and executing the Alice observations. The Alice team acknowledges continuing support from NASA via Jet Propulsion Laboratory contract 1336850 to the Southwest Research Institute. This research has made use of the SIMBAD database, operated at CDS, Strasbourg, France.

REFERENCES

- Ackerman M., Biaume F., Kockarts G., 1970, *Planet. Space Sci.*, 18, 1639
- Acton C. H., 1996, *Planet. Space Sci.*, 44, 65
- Balsiger H. et al., 2007, *Space Sci. Rev.*, 128, 745
- Barucci, M. A. et al., 2016, *A&A*, 595, A102
- Bieler A. et al., 2015, *Nature*, 526, 678
- Bockelée-Morvan D. et al., 2016, *MNRAS*, 462, S170
- Brion C. E., Tan K. H., 1979, *J. Electron Spectrosc. Related Phenomena*, 17, 101
- Cairns R. B., Samson J. A. R., 1965, *J. Geophys. Res.*, 70, 99
- Chan W. F., Cooper G., Brion C. E., 1993, *Chem. Phys.*, 178, 401
- Chung C.-Y., Chew E. P., Cheng B.-M., Bahou M., Lee Y.-P., 2001, *Nuclear Instrum. Methods Phys. Res. A*, 467-468, 1572
- Coradini A. et al., 2007, *Space Sci. Rev.*, 128, 529
- Ditchburn R. W., 1955, *Proc. R. Soc. Lond.*, 229, 44
- Dulieu F., Minissale M., Bockelée-Morvan D., 2017, *A&A*, 597, A56
- Fahr A., Nayak A. K., 1994, *Chem. Phys.*, 189, 725
- Feldman P. D. et al., 2015, *A&A*, 583, A8
- Feldman P. D. et al., 2016, *ApJ*, 825, L8
- Fougere N. et al., 2016, *MNRAS*, 462, S156

Gentieu E. P., Mentall J. E., 1970, *Science*, 169, 681
 Gulkis S. et al., 2007, *Space Sci. Rev.*, 128, 561
 Hitchcock A. P., Brion C. E., van der Wiel M. J., 1980, *Chem. Phys.*, 45, 461
 Huebner W. F., Mukherjee J., 2015, *Planet. Space Sci.*, 106, 11
 Koch E. E., Skibowski M., 1971, *Chem. Phys. Lett.*, 9, 429
 Le Roy, L. et al., 2015, *A&A*, 583, A1
 Lee, S. et al., 2015, *A&A*, 583, A5
 Lombos B. A., Sauvageau P., Sandorfy C., 1967, *J. Molecular Spectrosc.*, 24, 253
 Markwardt C. B., 2009, in Bohlender D. A., Durand D., Dowler P., eds, *ASP Conf. Ser. 411, Astronomical Data Analysis Software and Systems XVIII*. Astron. Soc. Pac., San Francisco, p. 251
 Mentall J. E., Gentieu E. P., Kraus M., Neumann D., 1971, *J. Chem. Phys.*, 55, 5471
 Metzger P. H., Cook G. R., 1964, *J. Chem. Phys.*, 41, 642
 Mota R. et al., 2005, *Chem. Phys. Lett.*, 416, 152
 Mount G. H., Moos H. W., 1978, *ApJ*, 224, L35
 Mousis, O. et al., 2016, *ApJ*, 823, L41
 Nakayama T., Watanabe K., 1964, *J. Chem. Phys.*, 40, 588
 Okabe H., 1981, *J. Chem. Phys.*, 75, 2772
 Okabe H., Becker D. A., 1963, *J. Chem. Phys.*, 39, 2549
 Rubin M., Altwegg K., van Dishoeck E. F., Schwehm G., 2015, *ApJ*, 815, L11
 Schoen R. I., 1962, *J. Chem. Phys.*, 37, 2032
 Stark G., Yoshino K., Smith P. L., Ito K., 2007, *J. Quant. Spectrosc. Radiative Transfer*, 103, 67
 Stern S. A. et al., 2007, *Space Sci. Rev.*, 128, 507
 Sun H., Weissler G. L., 1955, *J. Chem. Phys.*, 23, 1160
 Taquet V., Furuya K., Walsh C., van Dishoeck E. F., 2016, *MNRAS*, 462, S99
 Watanabe K., Zelikoff M., 1953, *J. Opt. Soc. America*, 43, 753
 Watanabe K., Jursa A. S., 1964, *J. Chem. Phys.*, 41, 1650
 Wenger M. et al., 2000, *A&AS*, 143, 9
 Yoshino K., Esmond J. R., Sun W. H., Parkinson W. H., Ito K., Matsui T., 1996, *J. Quant. Spectrosc. Radiative Transfer*, 55, 53
 Yoshino K., Parkinson W. H., Ito K., Matsui T., 2005, *J. Molecular Spectrosc.*, 229, 238
 Zelikoff M., Watanabe K., 1953, *J. Opt. Soc. America*, 43, 756

APPENDIX A: BEST-FIT ABSORPTION PROFILES

Figures A1-A29 present best-fit absorption profiles for all targeted and archival stellar appulses, arranged chronologically. The top panel of each figure displays the normalized stellar flux (black) and 1σ uncertainty (gray), with best-fit ensemble absorption (solid brown line) overlaid. Absorption from individual species is shown with solid (H₂O, O₂, CO, CO₂, CH₄) or dashed (C₂H₂, C₂H₆, C₂H₄, C₄H₂, H₂CO) lines. The bottom panel of each figure displays the residual of the ensemble fit.

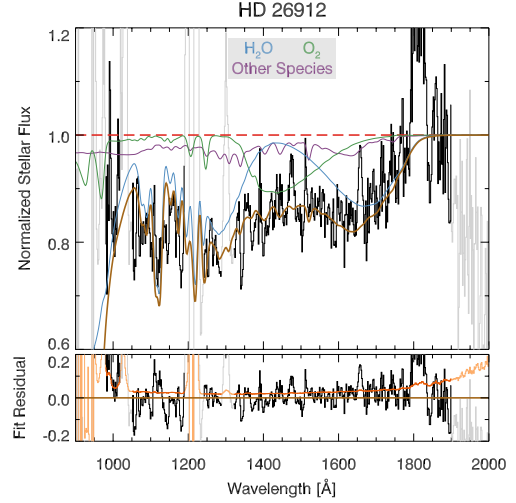


Figure A1. Fits to the appulse absorption of HD 26912 (FQ = 2).

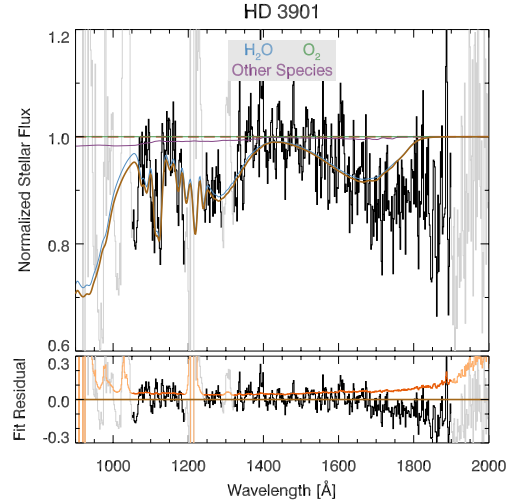


Figure A2. Fits to the appulse absorption of HD 3901 (FQ = 4).

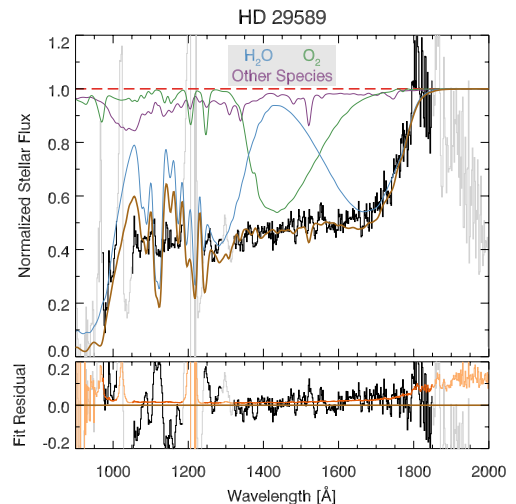


Figure A3. Fits to the appulse absorption of HD 29589 (FQ = 2).

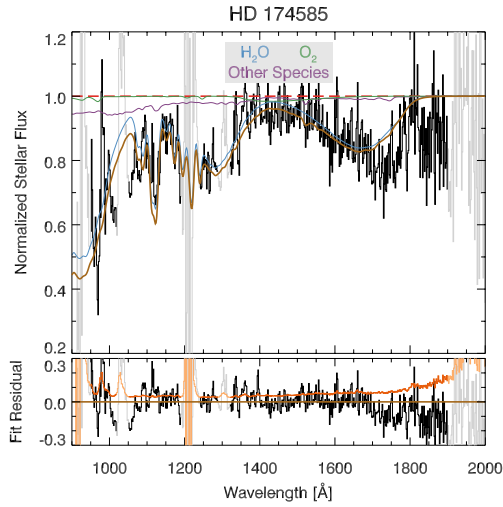


Figure A4. Fits to the appulse absorption of HD 174585 (FQ = 3).

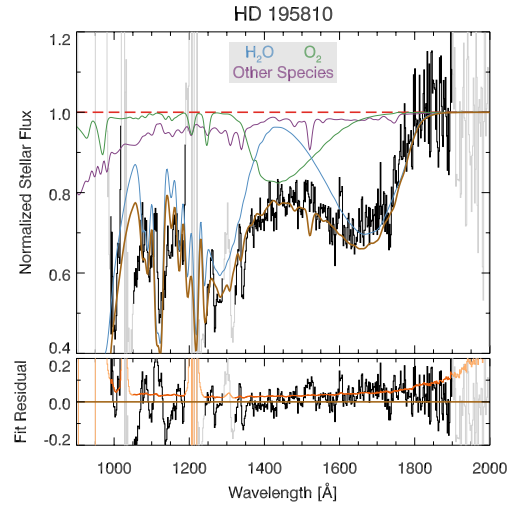


Figure A7. Fits to the appulse absorption of HD 195810 (FQ = 2).

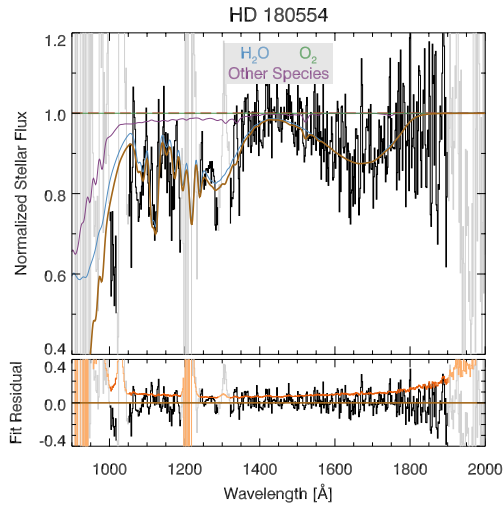


Figure A5. Fits to the appulse absorption of HD 180554 (FQ = 4).

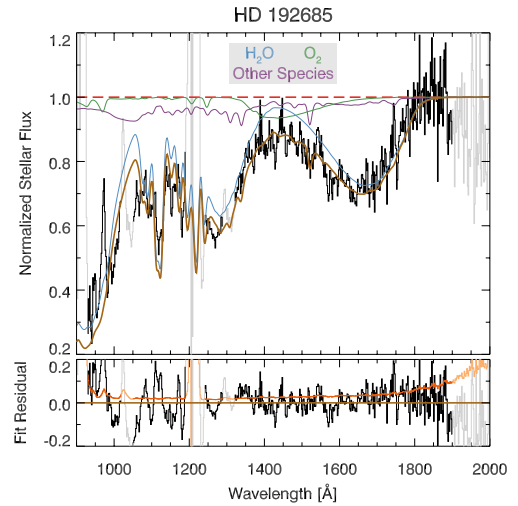


Figure A8. Fits to the appulse absorption of HD 192685 (FQ = 1).

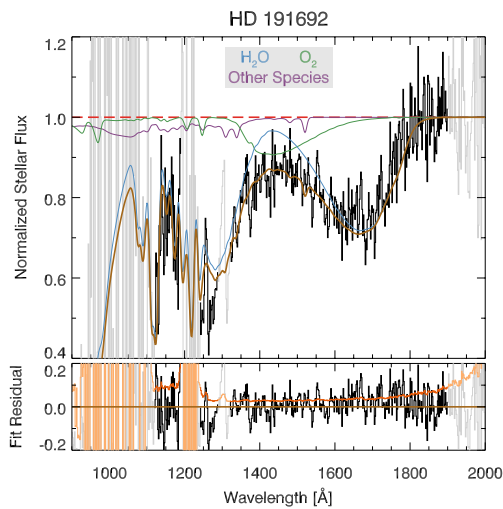


Figure A6. Fits to the appulse absorption of HD 191692 (FQ = 2).

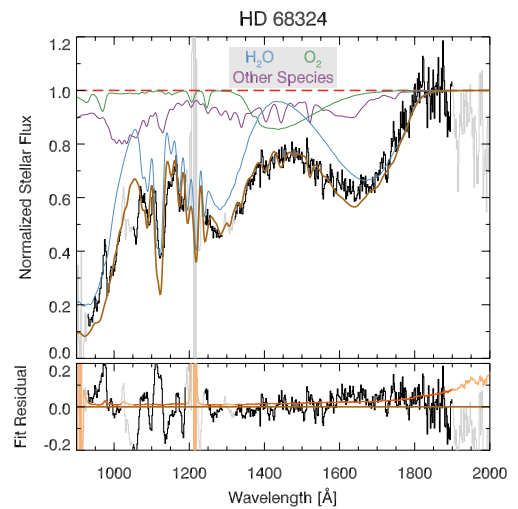


Figure A9. Fits to the appulse absorption of HD 68324 (FQ = 2).

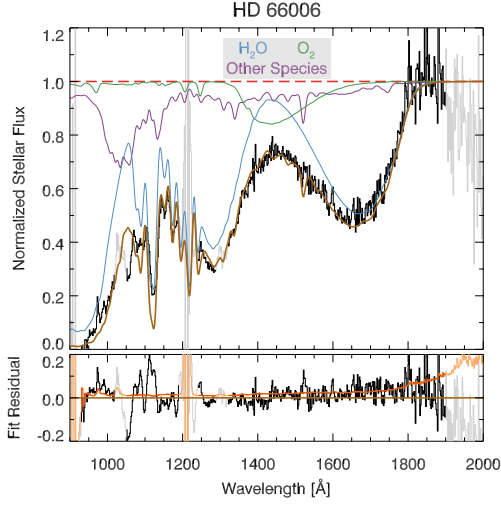


Figure A10. Fits to the appulse absorption of HD 66006 (FQ = 1).

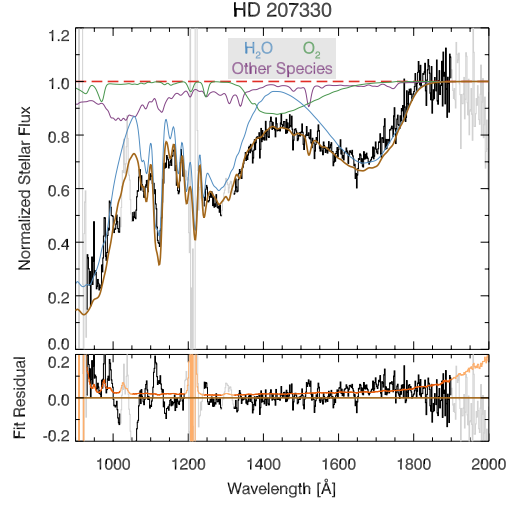


Figure A13. Fits to the appulse absorption of HD 207330 (FQ = 2).

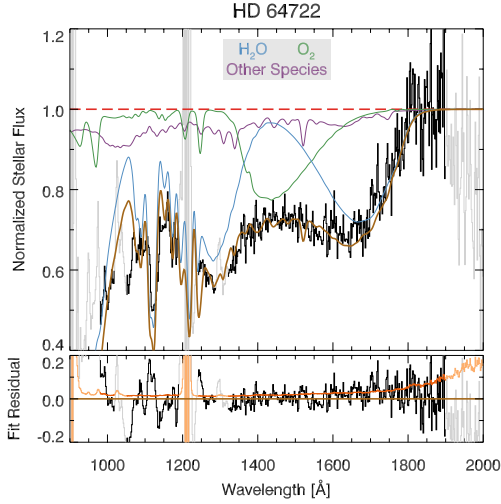


Figure A11. Fits to the appulse absorption of HD 64722 (FQ = 2).

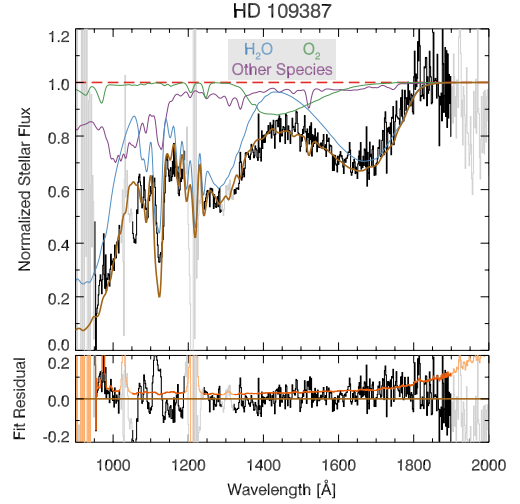


Figure A14. Fits to the appulse absorption of HD 109387 (FQ = 1).

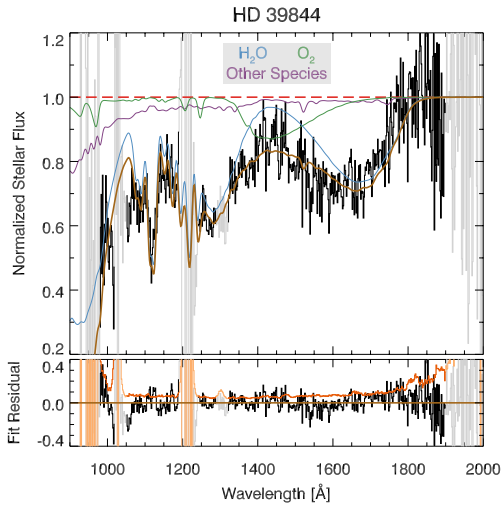


Figure A12. Fits to the appulse absorption of HD 39844 (FQ = 2).

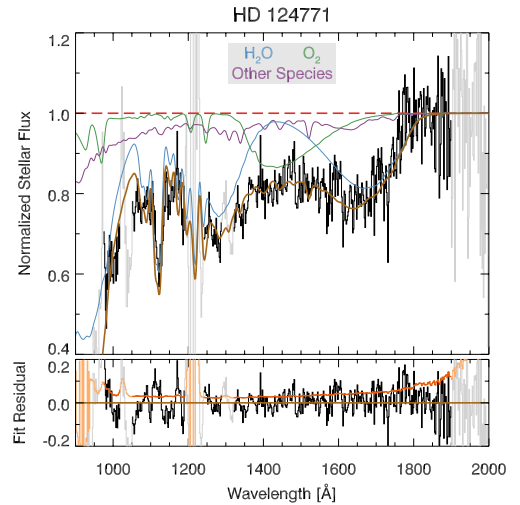


Figure A15. Fits to the appulse absorption of HD 124771 (FQ = 1).

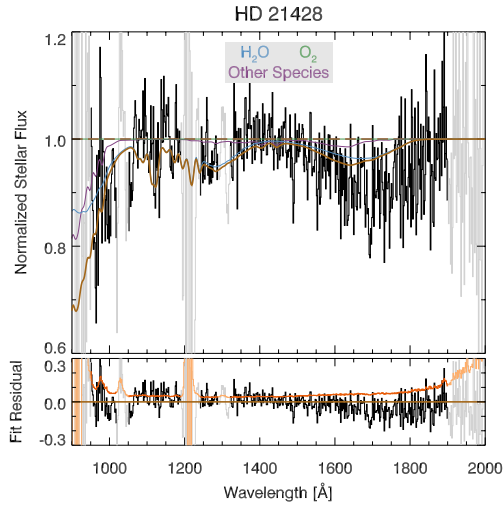


Figure A16. Fits to the appulse absorption of HD 21428 (FQ = 4).

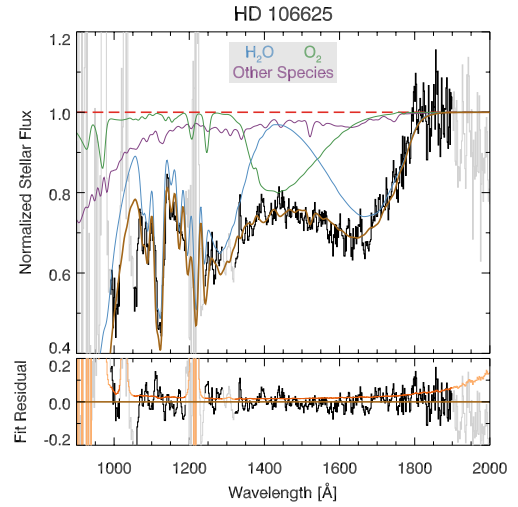


Figure A19. Fits to the appulse absorption of HD 106625 (FQ = 1).

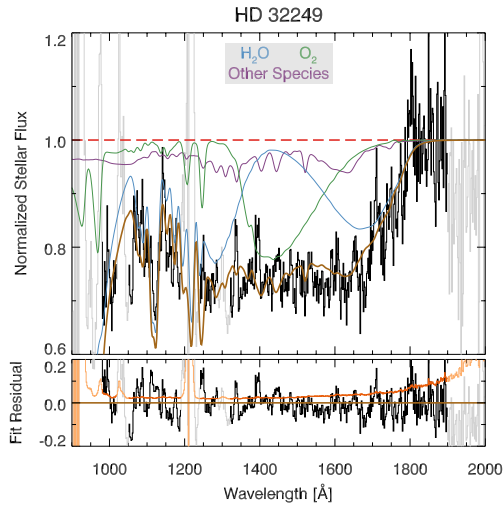


Figure A17. Fits to the appulse absorption of HD 32249 (FQ = 2).

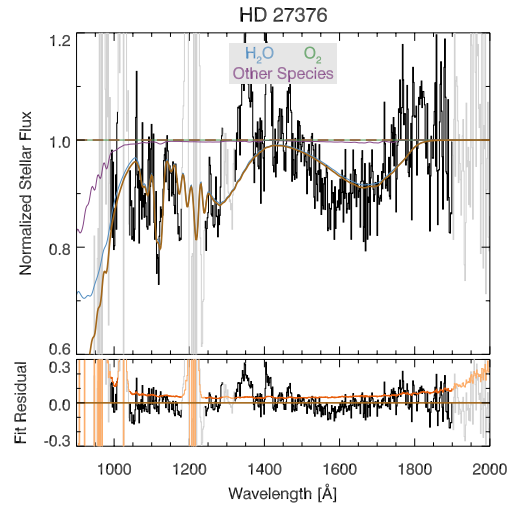


Figure A20. Fits to the appulse absorption of HD 27376 (FQ = 3).

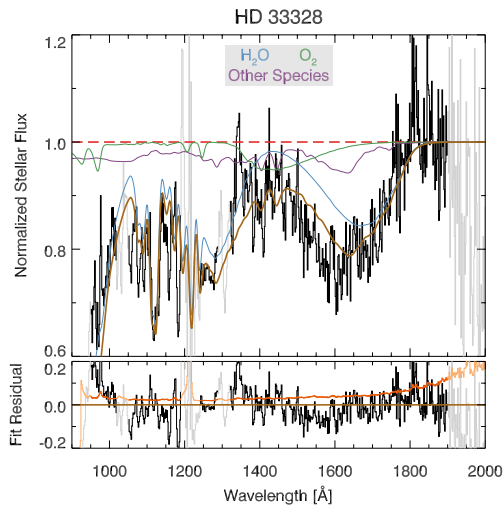


Figure A18. Fits to the appulse absorption of HD 33328 (FQ = 2).

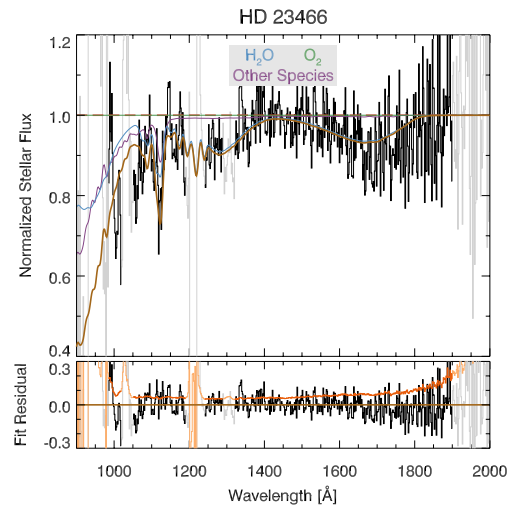


Figure A21. Fits to the appulse absorption of HD 23466 (FQ = 4).

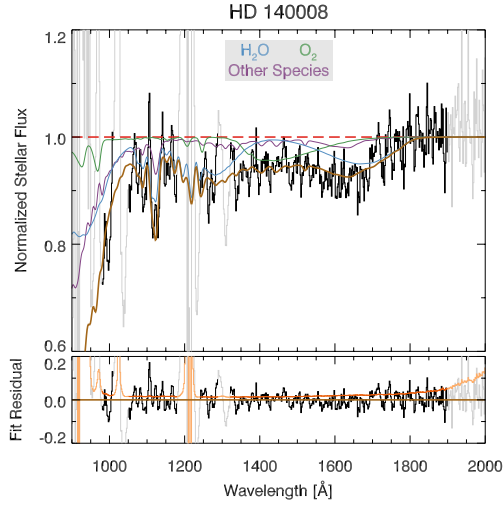


Figure A22. Fits to the appulse absorption of HD 140008 (FQ = 2).

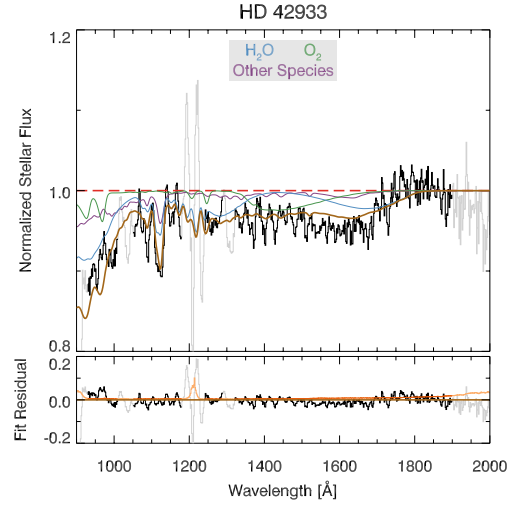


Figure A25. Fits to the appulse absorption of HD 42933 (FQ = 3).

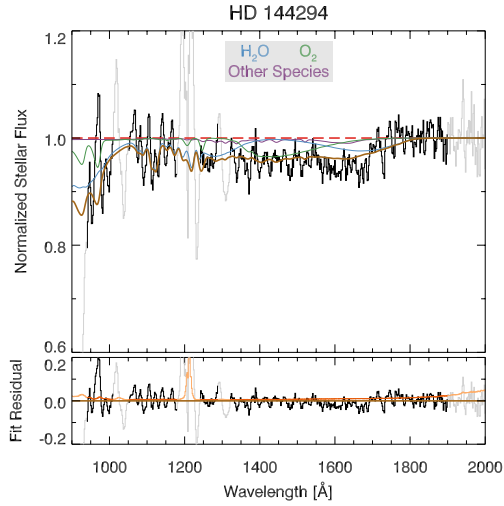


Figure A23. Fits to the appulse absorption of HD 144294 (FQ = 3).

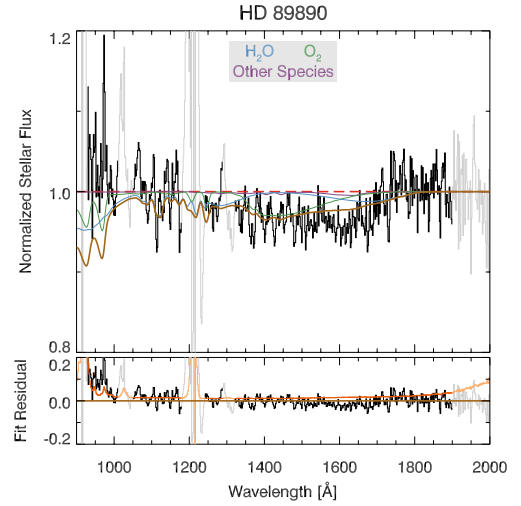


Figure A26. Fits to the appulse absorption of HD 89890 (FQ = 4).

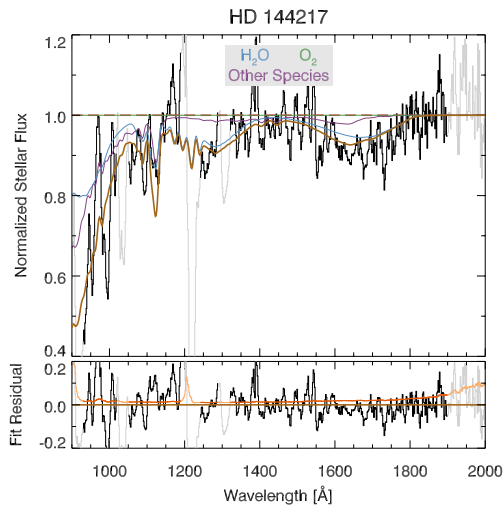


Figure A24. Fits to the appulse absorption of HD 144217 (FQ = 3).

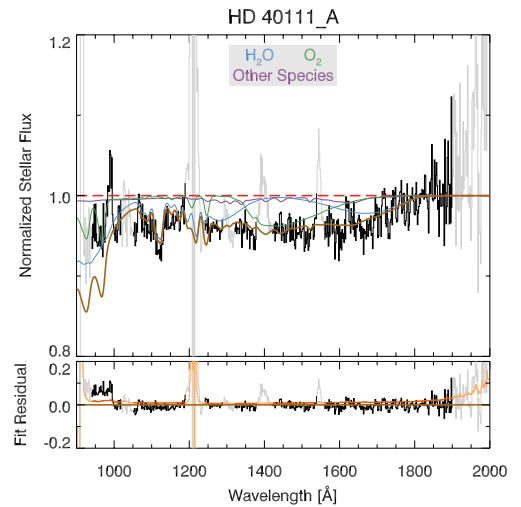


Figure A27. Fits to the first appulse absorption of HD 40111 (FQ = 3).

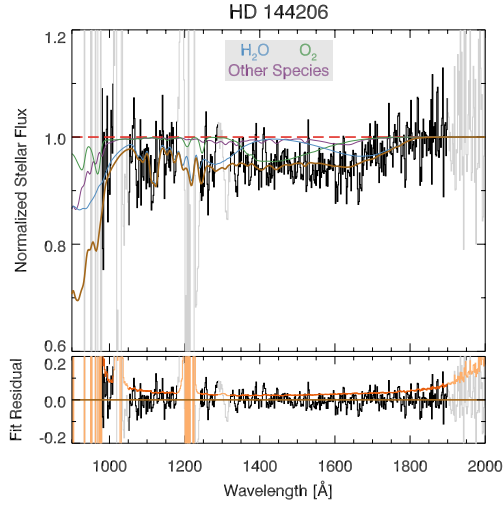


Figure A28. Fits to the appulse absorption of HD 144206 (FQ = 2).

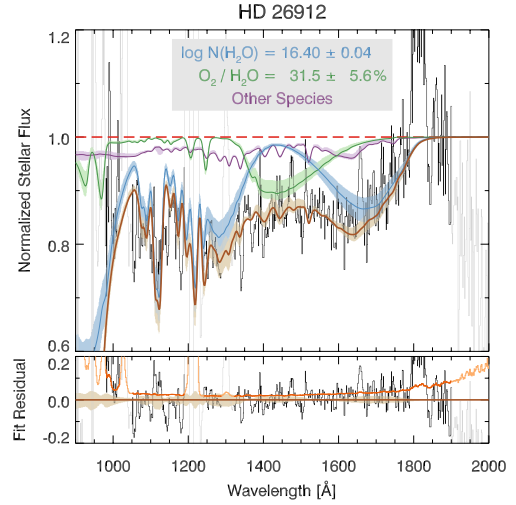


Figure B1. Adopted column densities for the appulse of HD 26912 (FQ = 2), with 95% (2σ) confidence bands.

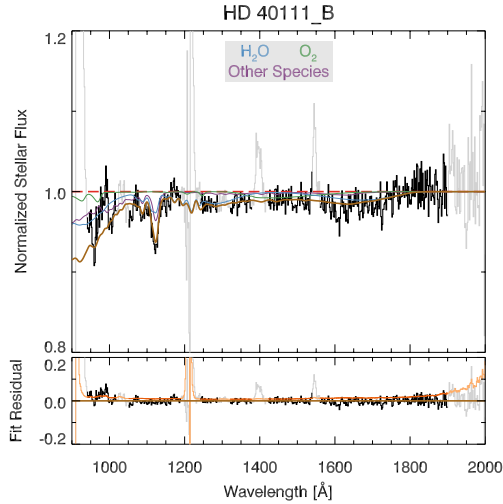


Figure A29. Fits to the second appulse absorption of HD 40111 (FQ = 3).

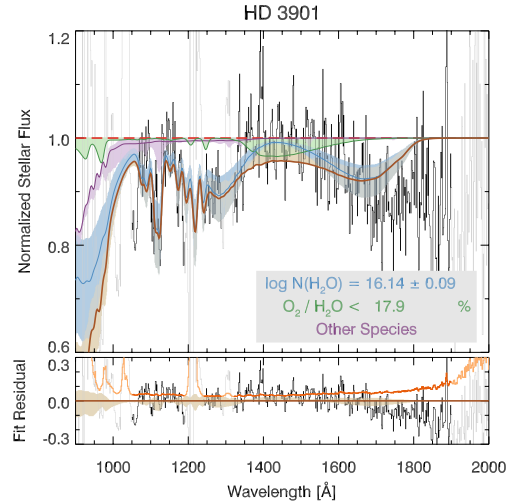


Figure B2. Adopted column densities for the appulse of HD 3901 (FQ = 4), with 95% (2σ) confidence bands.

APPENDIX B: ADOPTED ABSORPTION PROFILES

Figures B1-B29 present the adopted column densities for all targeted and archival stellar appulses, with 95% (2σ) confidence bands. The top panel of each figure displays the normalized stellar flux and associated 95% confidence band (gray), with ensemble fit (brown) and individual-species absorption overlaid using the adopted column densities of H_2O and O_2 from Table 4. The bottom panel of each figure displays the residual of the ensemble fit.

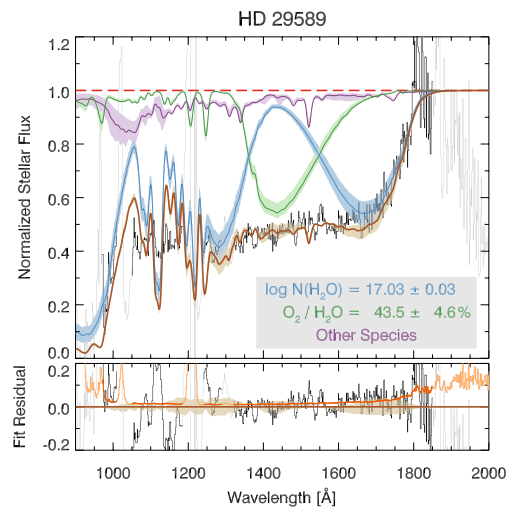


Figure B3. Adopted column densities for the appulse of HD 29589 (FQ = 2), with 95% (2σ) confidence bands.

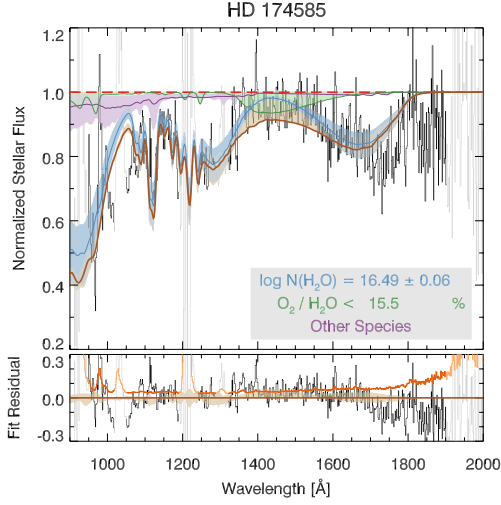


Figure B4. Adopted column densities for the appulse of HD 174585 (FQ = 3), with 95% (2σ) confidence bands.

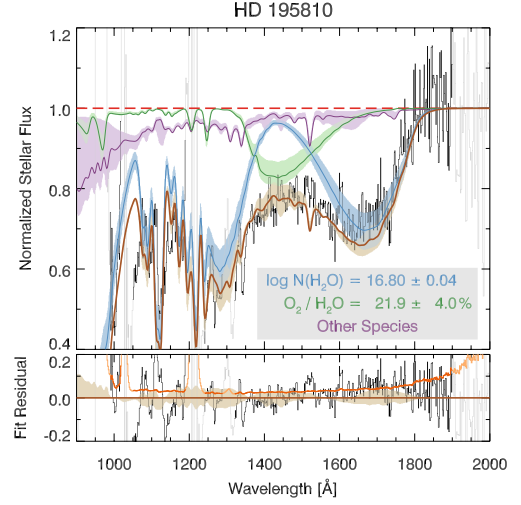


Figure B7. Adopted column densities for the appulse of HD 195810 (FQ = 2), with 95% (2σ) confidence bands.

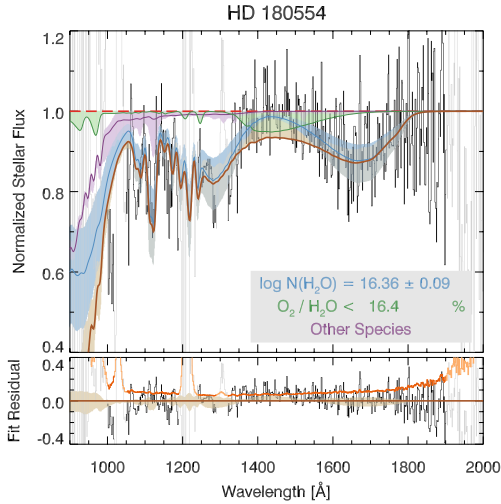


Figure B5. Adopted column densities for the appulse of HD 180554 (FQ = 4), with 95% (2σ) confidence bands.

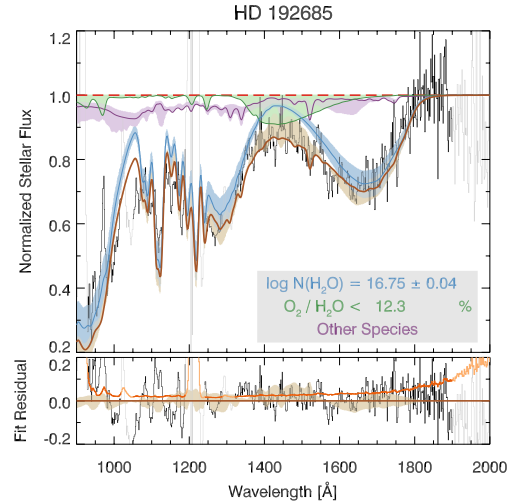


Figure B8. Adopted column densities for the appulse of HD 192685 (FQ = 1), with 95% (2σ) confidence bands.

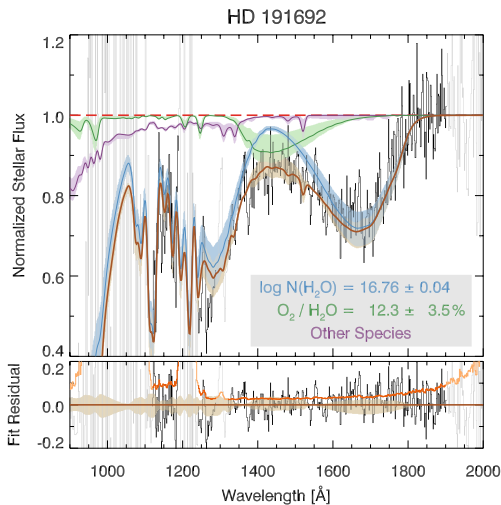


Figure B6. Adopted column densities for the appulse of HD 191692 (FQ = 2), with 95% (2σ) confidence bands.

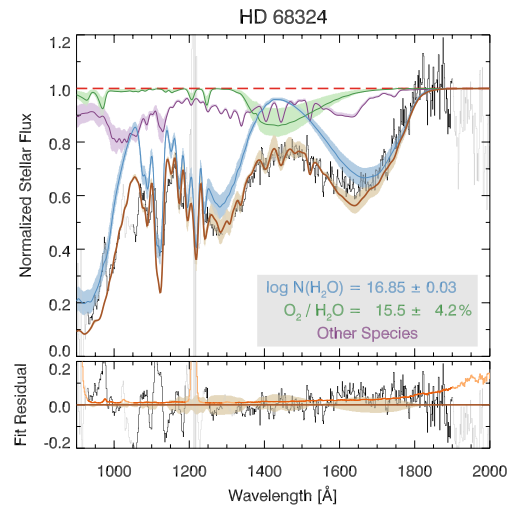


Figure B9. Adopted column densities for the appulse of HD 68324 (FQ = 2), with 95% (2σ) confidence bands.

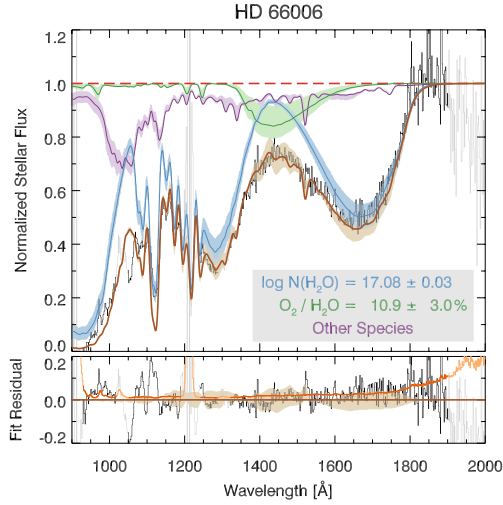


Figure B10. Adopted column densities for the appulse of HD 66006 (FQ = 1), with 95% (2σ) confidence bands.

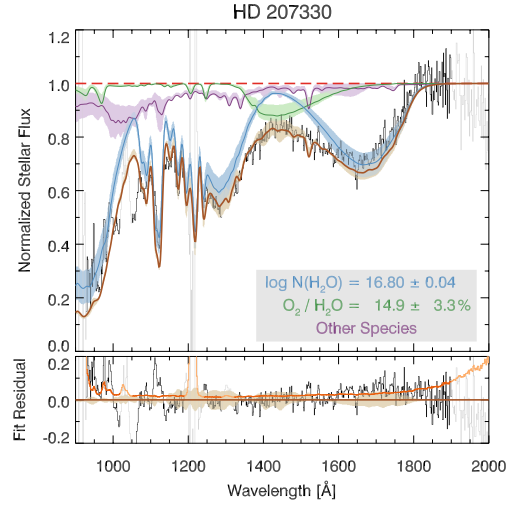


Figure B13. Adopted column densities for the appulse of HD 207330 (FQ = 2), with 95% (2σ) confidence bands.

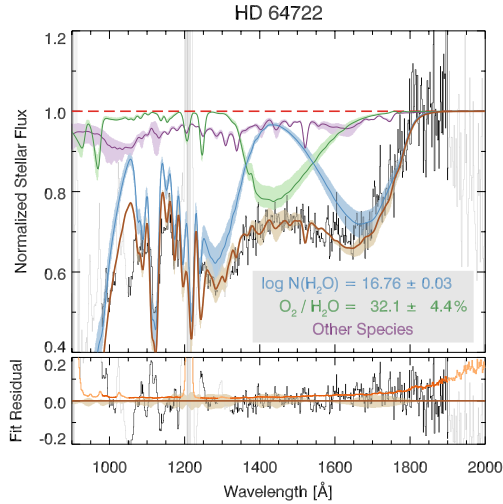


Figure B11. Adopted column densities for the appulse of HD 64722 (FQ = 2), with 95% (2σ) confidence bands.

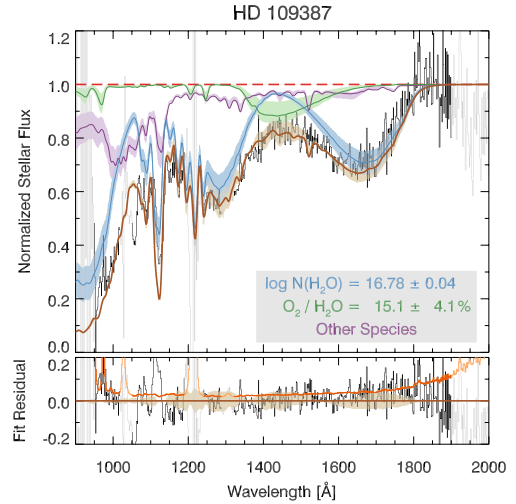


Figure B14. Adopted column densities for the appulse of HD 109387 (FQ = 1), with 95% (2σ) confidence bands.

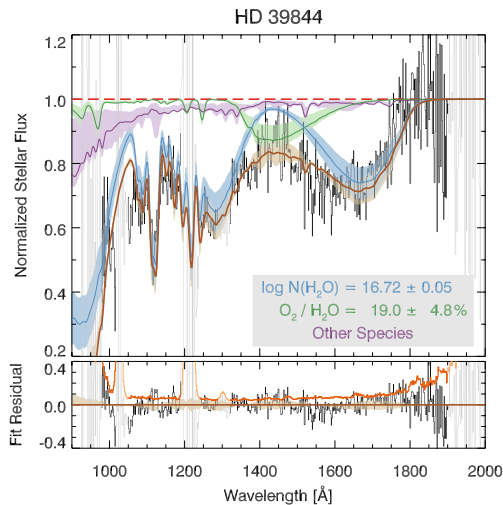


Figure B12. Adopted column densities for the appulse of HD 39844 (FQ = 2), with 95% (2σ) confidence bands.

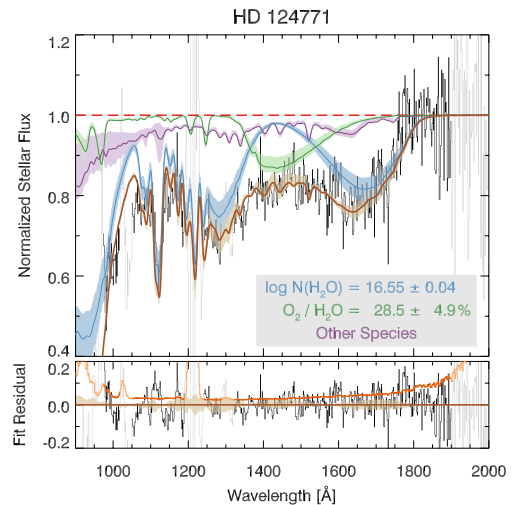


Figure B15. Adopted column densities for the appulse of HD 124771 (FQ = 1), with 95% (2σ) confidence bands.

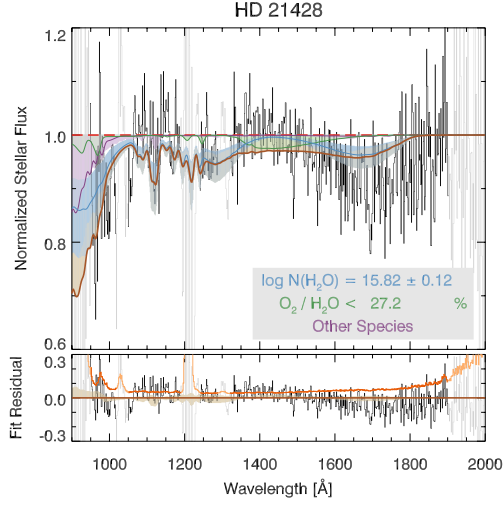


Figure B16. Adopted column densities for the appulse of HD 21428 (FQ = 4), with 95% (2σ) confidence bands.

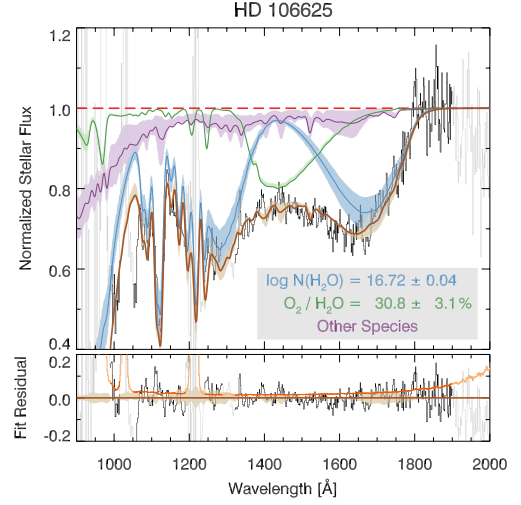


Figure B19. Adopted column densities for the appulse of HD 106625 (FQ = 1), with 95% (2σ) confidence bands.

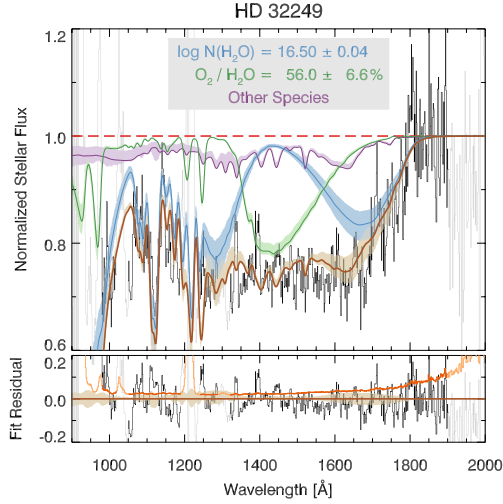


Figure B17. Adopted column densities for the appulse of HD 32249 (FQ = 2), with 95% (2σ) confidence bands.

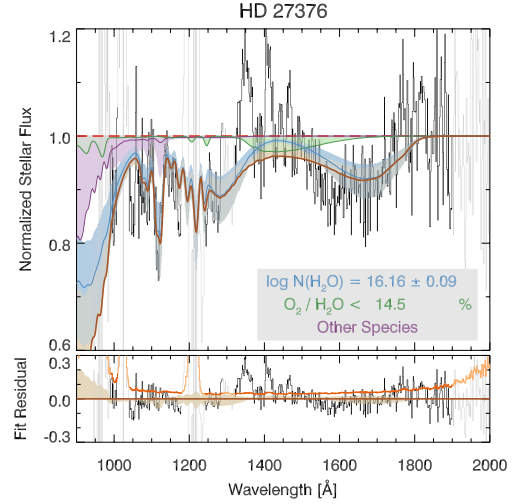


Figure B20. Adopted column densities for the appulse of HD 27376 (FQ = 3), with 95% (2σ) confidence bands.

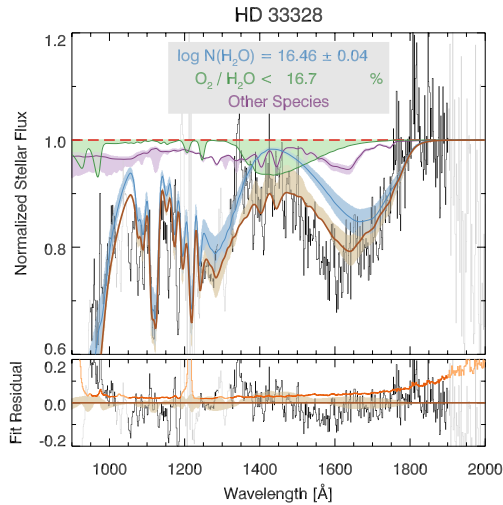


Figure B18. Adopted column densities for the appulse of HD 33328 (FQ = 2), with 95% (2σ) confidence bands.

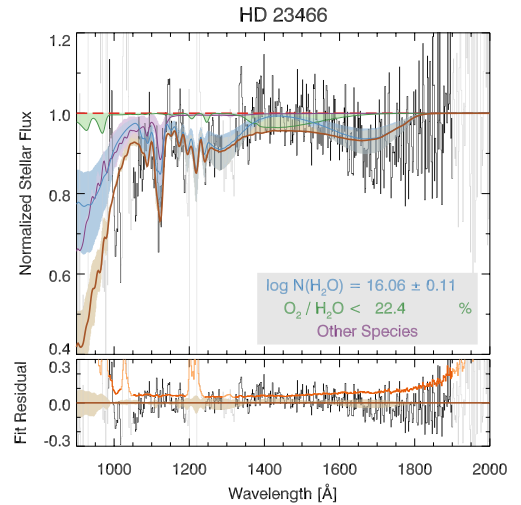


Figure B21. Adopted column densities for the appulse of HD 23466 (FQ = 4), with 95% (2σ) confidence bands.

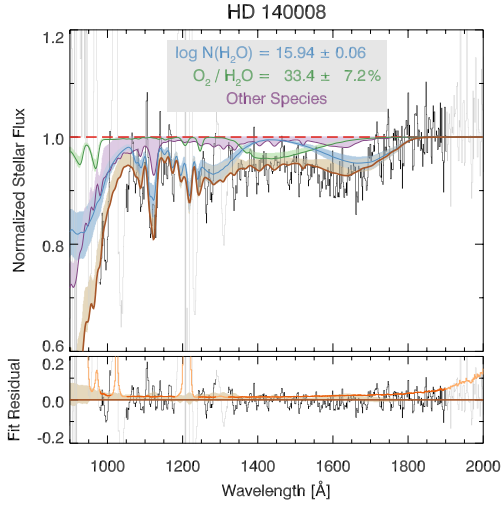


Figure B22. Adopted column densities for the appulse of HD 140008 (FQ = 2), with 95% (2σ) confidence bands.

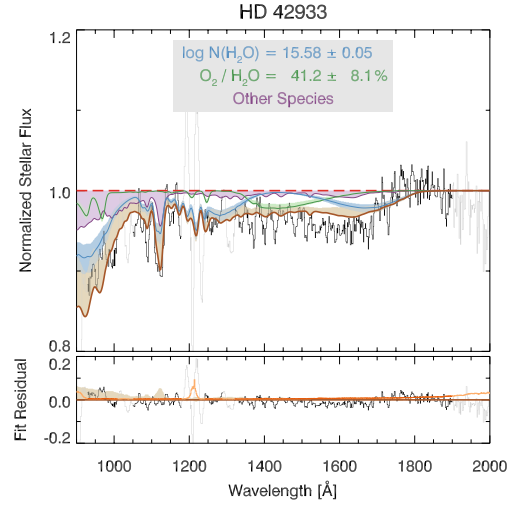


Figure B25. Adopted column densities for the appulse of HD 42933 (FQ = 3), with 95% (2σ) confidence bands.

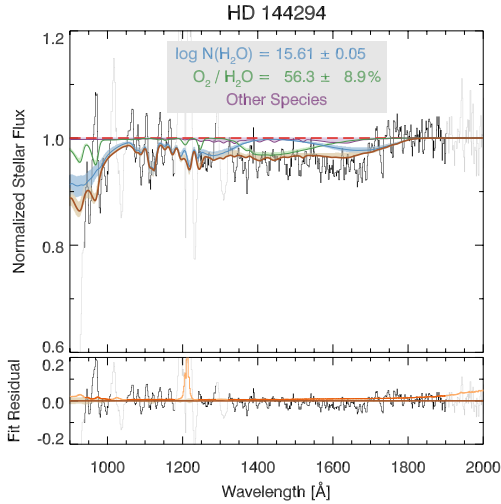


Figure B23. Adopted column densities for the appulse of HD 144294 (FQ = 3), with 95% (2σ) confidence bands.

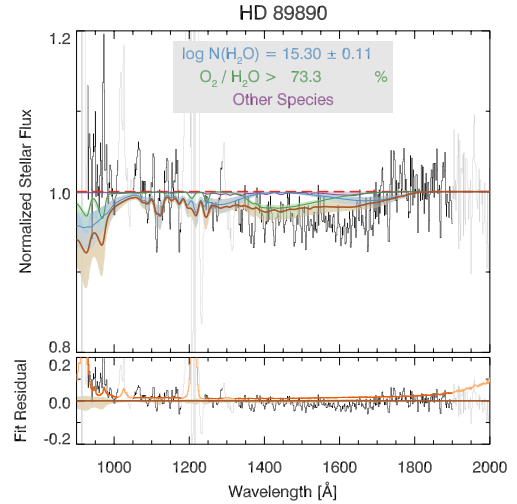


Figure B26. Adopted column densities for the appulse of HD 89890 (FQ = 4), with 95% (2σ) confidence bands.

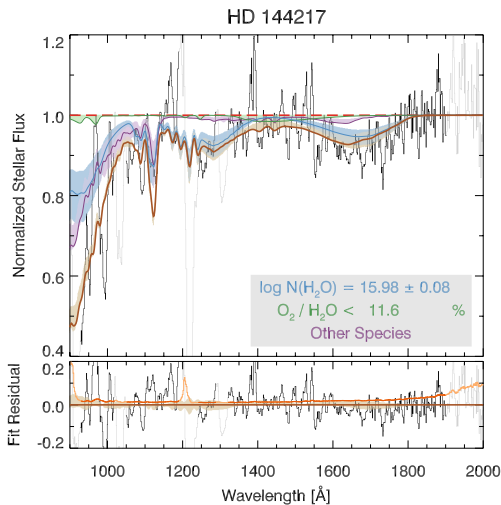


Figure B24. Adopted column densities for the appulse of HD 144217 (FQ = 3), with 95% (2σ) confidence bands.

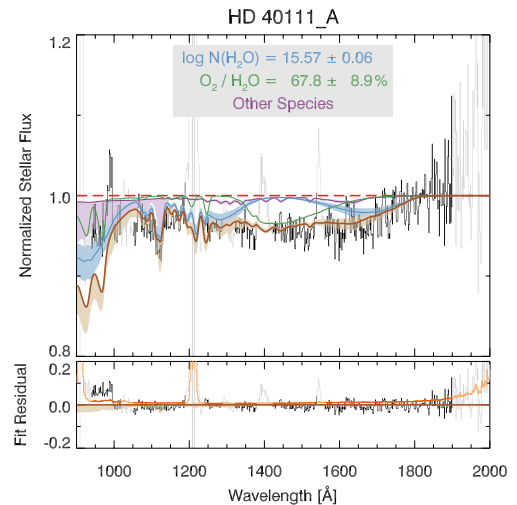


Figure B27. Adopted column densities for the first appulse of HD 40111 (FQ = 3), with 95% (2σ) confidence bands.

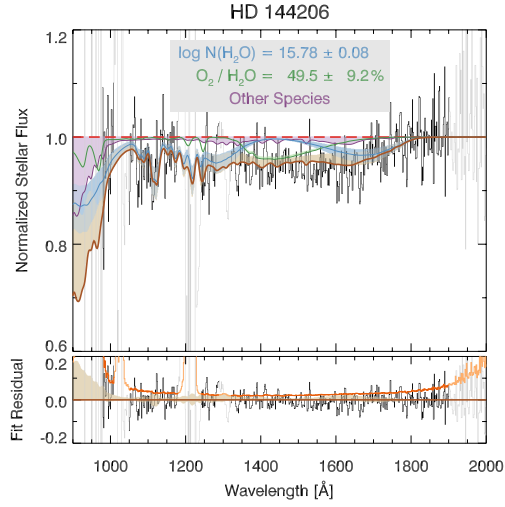


Figure B28. Adopted column densities for the appulse of HD 144206 (FQ = 2), with 95% (2σ) confidence bands.

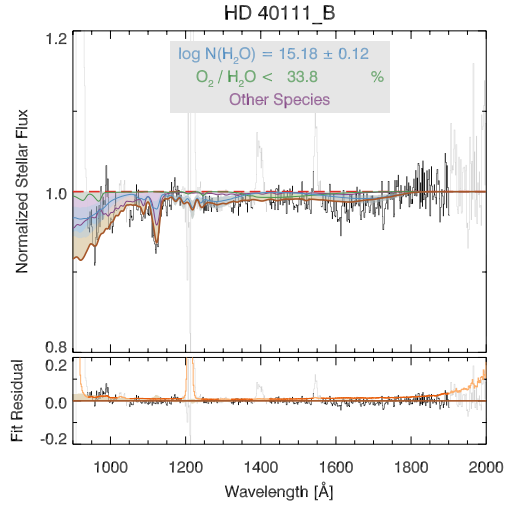


Figure B29. Adopted column densities for the second appulse of HD 40111 (FQ = 3), with 95% (2σ) confidence bands.

This paper has been typeset from a $\text{T}_{\text{E}}\text{X}/\text{L}^{\text{A}}\text{T}_{\text{E}}\text{X}$ file prepared by the author.